

AFAPL-TR-69-13

AD 692101

DIAGNOSTICS OF LOW-SPECIFIC-CHARGE COLLOID ION BEAM

JACK W. GEIS

TECHNICAL REPORT AFAPL-TR-69-13

JUNE 1969

AUG 28 1969

This document has been approved for public release and sale;
its distribution is unlimited.

AIR FORCE AERO PROPULSION LABORATORY
AIR FORCE SYSTEMS COMMAND
WRIGHT-PATTERSON AIR FORCE BASE, OHIO

1
CLEARINGHOUSE
U.S. GOVERNMENT PRINTING OFFICE
WASHINGTON, D.C. 20540

AFAPL-TR-69-13

DIAGNOSTICS OF LOW-SPECIFIC-CHARGE COLLOID ION BEAM

JACK W. GEIS

This document has been approved for public release and sale;
its distribution is unlimited.

FOREWORD

The analysis reported herein was performed as an in-house effort by the author for the Aerospace Power Division, Air Force Aero Propulsion Laboratory, Wright-Patterson Air Force Base, Ohio. The work was accomplished under Task 31402, Project 3141, Electric Propulsion Technology. The diagnostics program was conducted from June 1967 to January 1969. This report was submitted by the author in February 1969.

This report has been reviewed and is approved.

Philip E. Stover

PHILIP E. STOVER
Chief, Propulsion and Power Branch
Aerospace Power Division

ABSTRACT

As part of an in-house colloid diagnostic program, the first detailed mapping of propellant mass flow distribution from a colloid source has been completed, and the program has shown the influence of anisotropic or non-uniform flow conditions within the beam on the efficiency of source operation. The operating conditions of high propellant feed pressure, low voltage, and high resistivity of the sodium iodide/glycerol propellant, which created a very low specific charge beam, caused a nonuniform distribution of specific charge and beam current as a function of beam divergence half angle. The assumption of uniform beam conditions would result in a 12% error in computing thrust and a 25% error in determining overall efficiency.

TABLE OF CONTENTS

SECTION	PAGE
I INTRODUCTION	1
II THE SPECIFIC IMPULSE PARAMETER	2
III THE COLLOID ION ENGINE	5
IV DETERMINATION OF COLLOID CHARGE TO MASS DISTRIBUTION (ISOTROPIC)	8
1. The Time-Of-Flight Spectrometer	8
2. Determination of \bar{t} and \bar{t}^2 From TOF Measurements	14
3. Assumptions Made for Conventional Calculation of Engine Parameters	16
V DETERMINATION OF THRUSTOR PERFORMANCE CHARACTERISTICS BASED ON ANISOTROPIC CONDITIONS	19
VI EXPERIMENTAL SETUP AND PROCEDURES	23
1. Segmented Hemispherical Collector	23
2. Boom Collector	23
3. Geared Ball Current Collector (BC)	26
4. Total Current Collector (TC)	26
5. Colloid Source	29
6. Vacuum Chamber and TOF Scope Systems	32
VII RESULTS OF DIAGNOSTIC TESTS	36
1. Taking the Data	37
2. Test II (Three-Needle Array)	37
VIII CONCLUSIONS	70
IX RECOMMENDATIONS	71
APPENDIX DIGITAL COMPUTER PROGRAM DEVELOPED FOR CALCULATING COLLOID ENGINE PERFORMANCE	73
REFERENCES	77

ILLUSTRATIONS

FIGURE		PAGE
1.	System Weight Comparison for Electrical Thrusters	4
2.	Simplified Schematic of Colloid Engine	6
3.	Specific Impulse of Uniformly Charged Colloid Beam	7
4.	Oscilloscope Display of TOF Decay	9
5.	TOF Trace	13
6.	Possible Current, Specific Charge, and Propellant Mass Flow Distributions	18
7.	Geometry of Source Collector	20
8.	Possible TOF Collector Designs	24
9.	Positions of Collector Boom Pointer and Movable Plate for Locating Boom Collector	25
10.	Geared Ball Current Collector (BC) Assembly	27
11.	Controls for Positioning Geared Ball Current Collector Assembly	28
12.	Single-Needle Source and Movable Total Current Collector (TC) Assembly	30
13.	Controls for Moving Total Current Collector Assembly and for Positioning Extractor	31
14.	View of Single-Needle Colloid Source, Total Current Collector, and Ball Current Collector, Inside Vacuum Chamber	33
15.	Colloid Source Diagnostic Setup	34
16.	Colloid Source TOF Collector Electrical Schematic	35
17.	Single-Needle Ball Current Collector (BC) TOF Trace: $L = 5"$, $\beta = 25^\circ$, $\alpha = 150^\circ$, $\bar{c}\beta\alpha = 171$ Coulombs/Kg	38
18.	Three-Needle Array Total Current (TC) TOF Trace: $L = 1.95"$, $\bar{c} = 24.2$ Coulombs/Kg	38
19.	Three-Needle Array Ball Current Collector (BC) TOF Trace: $L = 5"$, $\beta = 25^\circ$, $\alpha = 30^\circ$, $\bar{c}\beta\alpha = 66.6$ Coulombs/Kg, $\bar{c} = 63.8$ Coulombs/Kg	39

ILLUSTRATIONS (Contd)

FIGURE		PAGE
20.	Various Positions of Ball Current Collector for Taking Data	40
21.	Beam Current Measured at Ball Current Collector as a Function of Azimuthal Angle, α , for $\beta = 25^\circ$	41
22.	Specific Charge, Determined from Ball Collector TOF Traces, as a Function of Azimuthal Angle α for $\beta = 25^\circ$	42
23.	Propellant Mass Flow, Calculated at the Ball Collector as a Function of Azimuthal Angle, α for $\beta = 25^\circ$	43
24.	Propellant Mass Flow Density, Calculated at the Ball Collector, as a Function of Azimuthal Angle, α for $\beta = 25^\circ$	45
25.	Determination of Surface Area of Circular Strip of Width, ΔS , and Radius, R	47
26.	Propellant Mass Flow Distribution Contributed by Elemental Surface Areas, ΔA , Situated at Different Beam Divergence Angles, β	48
27.	Mean Specific Charge \bar{c}_β , and Mean Root Specific Charge, $\bar{c}_\beta^{1/2}$, as a Function of Beam Divergence Angle, β	50
28.	Model of Three-Needle Array Propellant Mass Flow Distribution. Rods lengths are Proportional to Propellant Flow Rate	51
29.	Pattern of Propellant Deposited on Total Current Collector	52
30.	Photon Meter for Determining Ball Collector Screen Transparency	54
31.	Schematic of Ball Current Collector Showing Regions of Charged Particle Impact	56
32.	System Currents in Microamperes	60
33.	Influence of Needle Voltage on Specific Charge for Constant Feed System Pressure (TC, TOF, Trace)	62
34.	Thrust Distribution in Axial Direction Contributed by Elemental Surface Areas, ΔA , Situated at Different Beam Divergence Angles, β	65

SYMBOLS

I_{sp}	specific impulse, in seconds
F	thrust, in pounds
\dot{W}_p	propellant weight flow, in lbs/sec = $g_0 \dot{M}_p$
P_t	total input power, in kilowatts
P_{in}	beam power, in kilowatts
α_p	power supply specific weight, in pounds of power supply per kilowatt output
t_b	thrust time, in seconds
η	electrical efficiency in percent
Imp	total impulse, in pounds-seconds
v	velocity, in meters/sec
V	applied potential, in volts
V^-	extractor voltage
g_0	gravitational constant = 9.81 meters/sec ²
$q/m = c$	charge-to-mass ratio (specific charge), in coulombs/kilogram
L	time-of-flight distance between source and collector, in meters
\bar{c}	average or mean specific charge, in coulombs/kilogram
t	time, in seconds
$\bar{c}^{1/2}$	mean root specific charge
$(\bar{c}^{1/2})^2$	square mean root specific charge
β	beam divergence half angle
α	angle measured around beam axis
γ	secondary electron coefficient
m	particle mass
ρ	particle density = 1.26×10^3 kg/m ³

SYMBOLS (Contd)

r	particle radius
\bar{m}_β	average propellant mass flow density measured by ball current collector as a function of the angle β , in kg/sec-in ²
$m_{\beta a}$	propellant mass flow measured by ball collector at each data point, in, kg/sec
$i_{\beta a}$	current measured at ball collector at each data point, in amperes
$i_{scr(I)}$	screen current in Region <u>I</u>
i_{ext}	extractor current
$i_{hit\ ext}^+$	positive ion current striking extractor electrode
$i_{from\ ext}^-$	secondary electron current from extractor
i_{TC}	current read at total current collector
i_{BC}	current read at ball current collector
i_N	needle current
i_{total}^+	total positive-ion current emitted from source
\underline{I}	corresponds to cross-sectional area a of ball current collector schematic in Figure 31
\underline{II}	corresponds to cross-sectional area $(b-a)$ of ball current collector schematic in Figure 31
t_1	screen transparency for Region <u>I</u> of ball collector
t_2	screen transparency for Region <u>II</u> of ball collector
t_{avg}	average ball collector screen transparency
a	ball collector cross-sectional area = 0.249 in ²
b	projected cross-sectional area of screen = 0.477 in ²
$i_{thru\ scr(I)}^+$	positive ion current through ball collector screen in Region <u>I</u>
$i_{hit\ scr(I)}^+$	positive ion current striking ball collector screen in Region <u>I</u>

SYMBOLS (Contd)

Flow (1)	total flow to ball collector system in Region <u>I</u>
Flow (2)	total flow to ball collector system in Region <u>II</u> = $I_{scr}^{hit} (II)$
$I_{scr}^{+} (2)$	positive ion current thru ball collector screen in Region <u>II</u> , striking back metal plate
$I_{scr}^{hit} (2)$	positive ion current striking ball collector screen in Region <u>II</u>
$I_{scr}^{-} (1)$	secondary electrons from screen in Region <u>I</u>
$I_{scr}^{-} (2)$	secondary electrons from screen and back metal plate in Region <u>II</u>
$I_{scr}^{hit} (II)$	positive ion current striking screen and back metal plate in Region <u>II</u>
η_o	overall efficiency
η_S	speed distribution efficiency
η_D	isotropic divergence efficiency
η_F	thrust efficiency

SECTION I

INTRODUCTION

For about 10 years, the Air Force and the National Aeronautics and Space Administration (NASA) have been conducting research and development, both in-house and contractually, on many types of electric propulsion thruster concepts. The purpose of this work is to develop space thrusters that will provide significant performance gains over present and future chemical thrusters by minimizing system weight and providing mission flexibility of thrust vectoring, throttling, precisely controlled impulse bits, and rapid cycling.

Electric engines, unlike the conventional rocket engines, require an external power source to accelerate propellant gases to high velocities. This additional power requirement and its associated added weight are power and weight penalties that must be offset by other electric thruster performance characteristics or electric engines will not be considered for space applications.

It is important, in order to define accurately performance gains for electric thrusters, to understand thoroughly the characteristics of the engine exhaust. The propellant mass flow distribution and velocity vector must be known precisely before the thrust vector can be computed and overall engine efficiency can be determined.

The purpose of this program was to determine the effects of beam current and charge-to-mass (specific charge) distributions on propellant mass flow distribution in a colloid ion engine source. These effects, if any, can be seen in the calculation of thrust, efficiency, and specific impulse.

SECTION II

THE SPECIFIC IMPULSE PARAMETER

One of the main performance advantages of many types of electric engines is the ability to operate over a broad range of "specific impulse." Let us define this term and briefly show how it affects engine performance (Reference 1).

Specific impulse is the length of time in seconds an engine can operate at a certain thrust level on a given amount of fuel. The higher the specific impulse value for a given thruster, the more economical that thruster is in using its propellant.

Specific impulse is defined as:

$$I_{sp} = F / \dot{W}_p \quad (1)$$

where

I_{sp} = specific impulse, in sec

F = thrust, in lbs

\dot{W}_p = propellant weight flow in lbs/sec

Total system weight for an electric thruster is given by

$$W_t = P_t \alpha_p + \dot{W}_p t_b \quad (2)$$

where

P_t = total input power to the electric thruster in kw

α_p = power supply specific weight, in lbs of power supply per kw output

W_t = total system weight, in lbs

t_b = thrust time, in sec

Since electric input power can be expressed as

$$P_t = F \text{ Isp } (10^2 / 45.9 \eta) \quad (3)$$

where

η = electrical efficiency in percent, Equation (2) can be expanded and we obtain

$$\begin{aligned} W_t &= F \text{ Isp } \times (10^2 \alpha_p / 45.9 \eta) + F (t_b / \text{Isp}) \\ &= F \text{ Isp } \times (10^2 \alpha_p / 45.9 \eta) + \text{Imp} / \text{Isp} \end{aligned} \quad (4)$$

where

Imp = mission-determined total impulse in lbs-sec.

Equations (2), (3), and (4) show that, for a mission-determined thrust and a specific weight for a given power supply, the total system weight is influenced by the engine efficiency, total impulse, and specific impulse. Total impulse is determined by the requirements for a specific mission. Equation (4) shows that the highest engine efficiency is always desirable in terms of minimizing system weight, but a trade-off occurs between power supply weight and total propellant weight as a function of Isp:

$$\begin{aligned} P_t &= f(\text{Isp}) \\ W_p &= f(1/\text{Isp}) \end{aligned}$$

Figure 1 shows a typical system weight trade-off.

A broad range of specific impulse is, therefore, of interest to the systems designer because of the tradeoffs he can make in achieving optimum system power and system weight. In general, these tradeoffs involve the parameters of thrust level, specific impulse, power supply weight, engine efficiency, and mission duration.

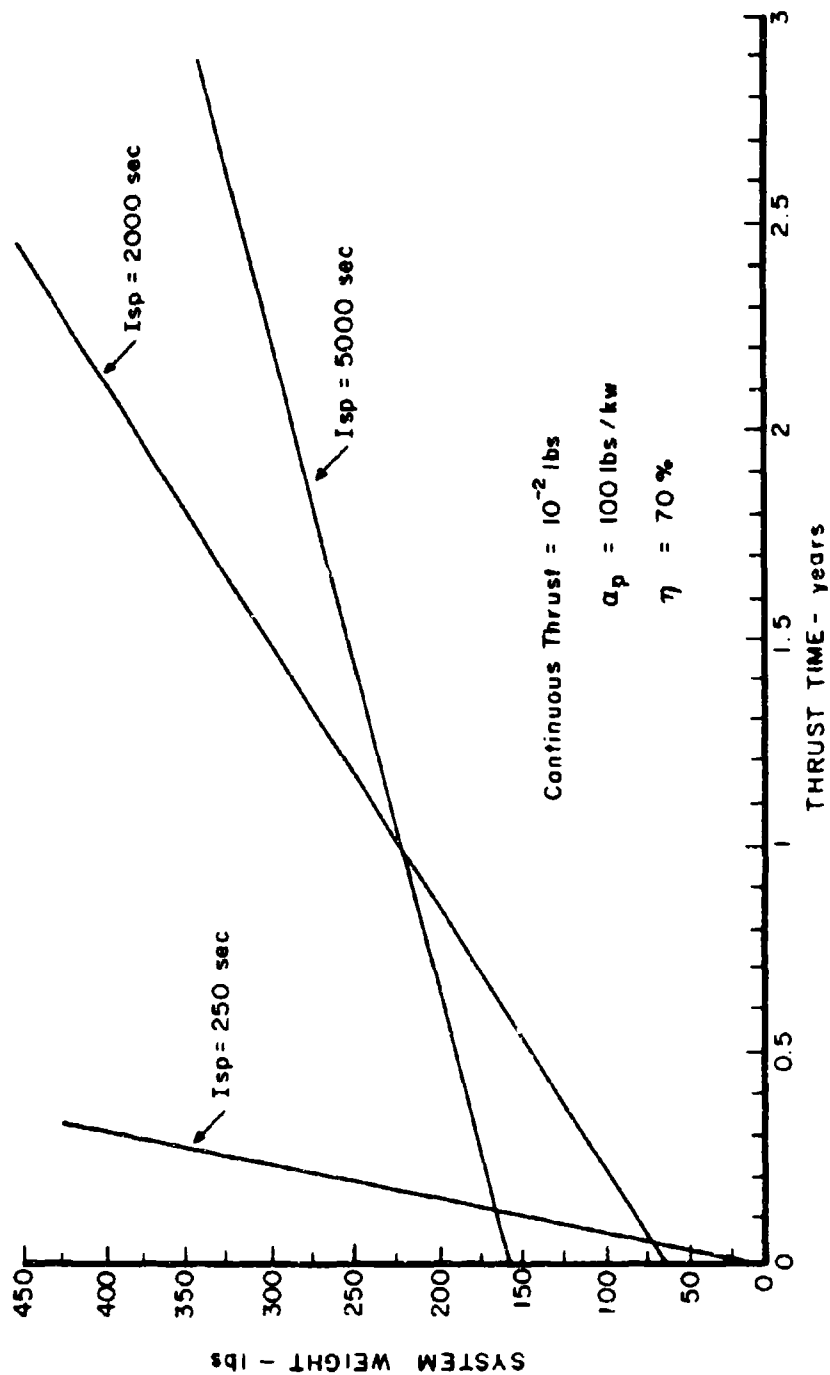


Figure 1. System Weight Comparison for Electric Thrusters

SECTION III

THE COLLOID ION ENGINE

The colloid ion engine is one type of electric propulsion device that offers high potential for operating efficiently and performing many useful missions in space. The following paragraphs briefly describe the principle of operation.

A conducting liquid passing through a fine metallic capillary tube is subjected to an intense electrostatic field as it reaches the tip of the capillary. This field is produced by raising the potential of the capillary with respect to a metallic plate containing a hole, the center of which lies on the axis of the capillary. If the electric field is high enough, the electric forces on the liquid exceeds the surface tension forces, and the liquid surface ruptures and forms small charged droplets called colloids. These charged droplets are then accelerated to high velocities by the field and pass through the aperture in the downstream electrode.

Beyond the downstream electrode, the charged droplets must be neutralized to prevent space charge buildup in the beam and resultant thrust reduction. Figure 2 shows a simplified schematic of a colloid engine.

The velocity of a charged particle is related by

$$v = \sqrt{2qV/m} = g_0 I_{sp}, \text{ in meters/sec} \quad (5)$$

where

V = applied potential in volts

q/m = represents the charge-to-mass ratio of the charged droplet
in coulombs/kg

g_0 = gravitational constant = 9.81 meters/sec²

The specific impulse obtainable by a colloid device, therefore, depends not only upon the applied potential, but upon the charge-to-mass distribution

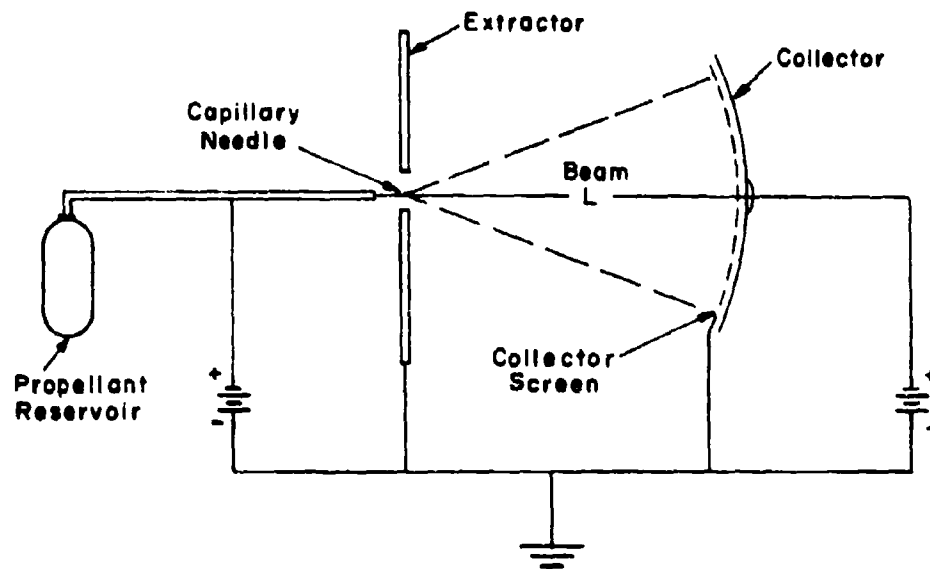


Figure 2. Simplified Schematic of Colloid Engine

in the beam. It will be shown later that the efficiency of a colloid engine, in large part, is also influenced by this distribution (Equation 23).

Figure 3 shows the charge-to-mass ratio (c) (specific charge) as a function of applied potential with specific impulse as a parameter.

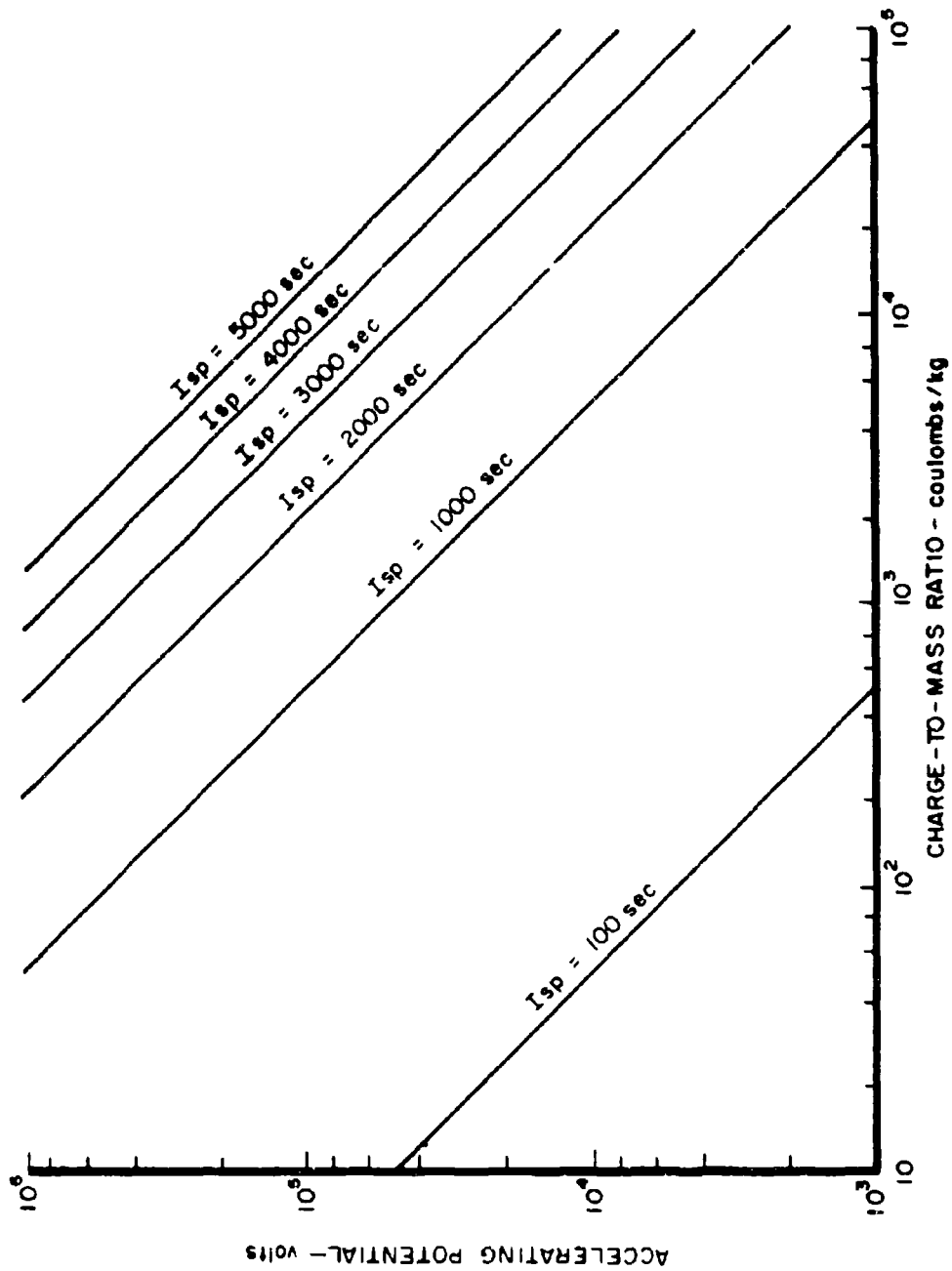


Figure 3. Specific Impulse of Uniformly Charged Colloid Beam

SECTION IV

DETERMINATION OF COLLOID CHARGE-TO-MASS
DISTRIBUTION (ISOTROPIC)

The charge-to-mass ratio of a colloid beam is not uniform from colloid particle to colloid particle but varies from several coulombs per kg to many thousands of coul/kg. A technique, therefore, must be used to determine the average or mean charge-to-mass ratio of the beam, \bar{c} .

1. THE TIME-OF-FLIGHT SPECTROMETER

In 1963, H. Shelton and E. Cohen developed a time-of-flight (TOF) spectrometer which permits the specific charge distribution (\bar{c}) of the entire beam to be measured instantaneously (Reference 2). The device works in the following way (Reference 3).

A shielded collector is located at a distance L from the colloid source as shown in Figure 2. Because of the electric field configuration at the needle tip, charged droplets reach their terminal velocities within a few millimeters and then travel at that velocity to the downstream collector. This particle velocity is given by Equation (5). Since all the droplets fall through the same potential, there will be a velocity distribution corresponding to the specific charge distribution in the beam. The current read at the collector is the sum of each of the individual specific charge species.

When the potential on the needle is pulsed to ground, no more charged droplets can be formed, and a current decay can be observed at the collector. Particle species having the highest value of \bar{c} and, therefore, the highest velocity, are the first to stop contributing to the collector current. When the last particle of this specie arrives at the collector, the current will drop to a lower level. The current will then continue to decay to lower levels as different \bar{c} species arrive at the collector (see Figure 4). In practice, specific charge distributions are equally continuous so that the decay is a continuous function, rather than the step function as shown.

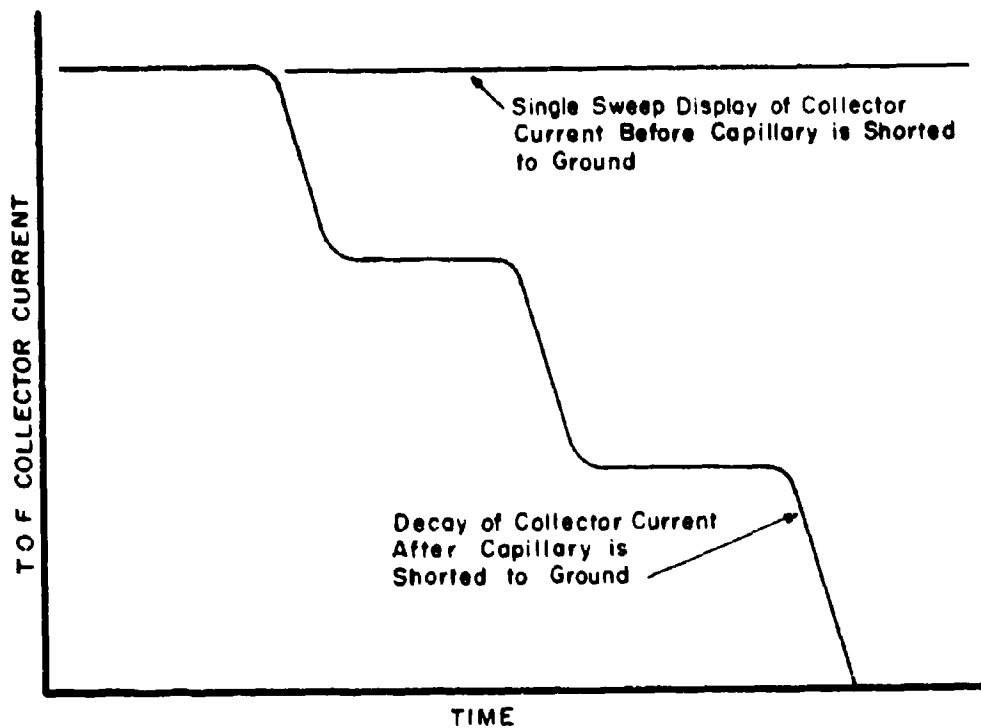


Figure 4. Oscilloscope Display of TOF Decay

The time at which the current decays to a new level represents the time required for the last particle of that specie to travel from needle to collector and is given by (Reference 3).

$$t = \frac{L}{v} = \frac{L}{\sqrt{2cV}} \quad (6)$$

$$c = \frac{L^2}{2Vt^2} \quad (7)$$

This represents the specific charge of a given specie in the beam.

To calculate the performance of a colloid needle one must know the mass weighted average of the specific charge distribution \bar{c} , the mean root value $\overline{c^{1/2}}$, and $(\overline{c^{1/2}})^2$, the square mean root specific charge.

\bar{c} can be determined as follows:

$$\bar{c} = \int_0^{\infty} c f(c) dc \quad (8)$$

where $f(c) = dm/\dot{M}dc = dI/\dot{M}cdc$ is the normalized mass distribution per unit specific charge (References 4 and 5) and $dm = dI/c$ for each specie.

Substituting in Equation (8), we find

$$\bar{c} = \frac{\int_0^{\infty} dI}{\int_0^{\infty} dm} = \frac{\int_0^{\infty} c dm}{\int_0^{\infty} dm} \quad (9)$$

Substituting in the value of c from Equation (7):

$$\bar{c} = \frac{\int_0^{\infty} dI}{\frac{2V}{L^2} \int_0^{\infty} t^2 dI} = \frac{I_0 L^2}{2V \int_0^{\infty} t^2 dI} \quad (10)$$

where I_0 is the current observed on the TOF collector at $t = 0$.

In like manner,

$$\bar{c} = \frac{\int_0^{\infty} c^{1/2} dm}{\int_0^{\infty} dm} = \frac{\int_0^{\infty} \frac{dI}{c^{1/2}}}{\int_0^{\infty} \frac{dI}{c}} \quad (11)$$

where

$$c = -\frac{L^2}{2Vt^2} \quad \text{as before and}$$

$$c^{1/2} = \frac{L}{(\sqrt{2Vt})}$$

By substituting in Equation (11), we find

$$\overline{c^{1/2}} = \frac{\frac{L}{\sqrt{2V}} \int_0^\infty t dI}{\int_0^\infty t^2 dI} \quad (12)$$

$$\overline{c^{1/2}}^2 = \frac{L^2}{2V} \frac{\left[\int_0^\infty t dI \right]^2}{\left[\int_0^\infty t^2 dI \right]^2} \quad (13)$$

Equations (10), (12), and (13) can be simplified by observing the relationships

$$\overline{t^2} = \int_0^\infty t^2 f(t) dt \quad (14)$$

and

$$\overline{t} = \int_0^\infty t f(t) dt \quad (15)$$

where

$$\begin{aligned} f(t) &= -\frac{1}{I_0} \frac{dI}{dt} \quad \text{or} \quad I = -\int_0^\infty I_0 f(t) dt \\ \therefore \overline{t^2} &= -\frac{1}{I_0} \int_0^\infty t^2 dI \end{aligned} \quad (16)$$

and

$$\overline{t} = -\frac{1}{I_0} \int_0^\infty t dI \quad (17)$$

We use these two relationships (Eqs. 16 and 17), and Equations (10), (12), and (13) become

$$\overline{c} = \frac{L^2}{2V \overline{t}^2} \quad (10')$$

$$\overline{c^{1/2}} = \frac{L}{\sqrt{2V}} \frac{\overline{t}}{\overline{t^2}} \quad (12')$$

$$\overline{c^{1/2}}^2 = \frac{L^2}{2V} \frac{(\overline{t})^2}{(\overline{t^2})^2} \quad (13')$$

References 3 and 5 derive the TOF determinations for \bar{t} and $\overline{t^2}$, so they will not be presented here. However, integration by parts of Equations (16) and (17) yields (see Figure 5)

$$\overline{t^2} = 2 \int_0^{t_f} \frac{I}{I_0} t dt \approx \sum_{n^*=1/2}^f 2n^* \frac{(\Delta t)^2}{I_0} I_n^* \quad (18)$$

$$\bar{t} = \int_0^{t_f} \frac{I}{I_0} dt \approx \sum_{n^*=1/2}^f \frac{I_n^* \Delta t}{I_0} \quad (19)$$

where

$$n^* = \frac{n_{j-1} + n_j}{2}$$

$$j = 1, 2, 3, \dots, f$$

The thrust obtained from a nondivergent colloid beam is

$$F = \dot{M} \bar{v} = \frac{I_0 \bar{v}}{c} = \frac{I_0}{c} \sqrt{2eV} = \frac{\sqrt{2V} I_0 c^{1/2}}{c} \quad (20)$$

Specific impulse is

$$I_{sp} = \frac{F}{\dot{M} g_0} = \frac{\sqrt{2V} c^{1/2}}{\dot{M} g_0} \quad (21)$$

The power in the beam is

$$P_{IN} = I_0 V \quad (22)$$

Therefore, thrust efficiency or (speed distribution efficiency) is

$$\eta_S = \eta_F = \frac{F^2}{2 \dot{M} P_{IN}} = \frac{(\bar{v} c^{1/2})^2}{c} = \frac{(\bar{v})^2}{v^2} \quad (23)$$

Thus, thrust efficiency is influenced by the specific charge distribution in the beam. If all the particles had the same charge-to-mass ratio, the speed efficiency would equal 100%.

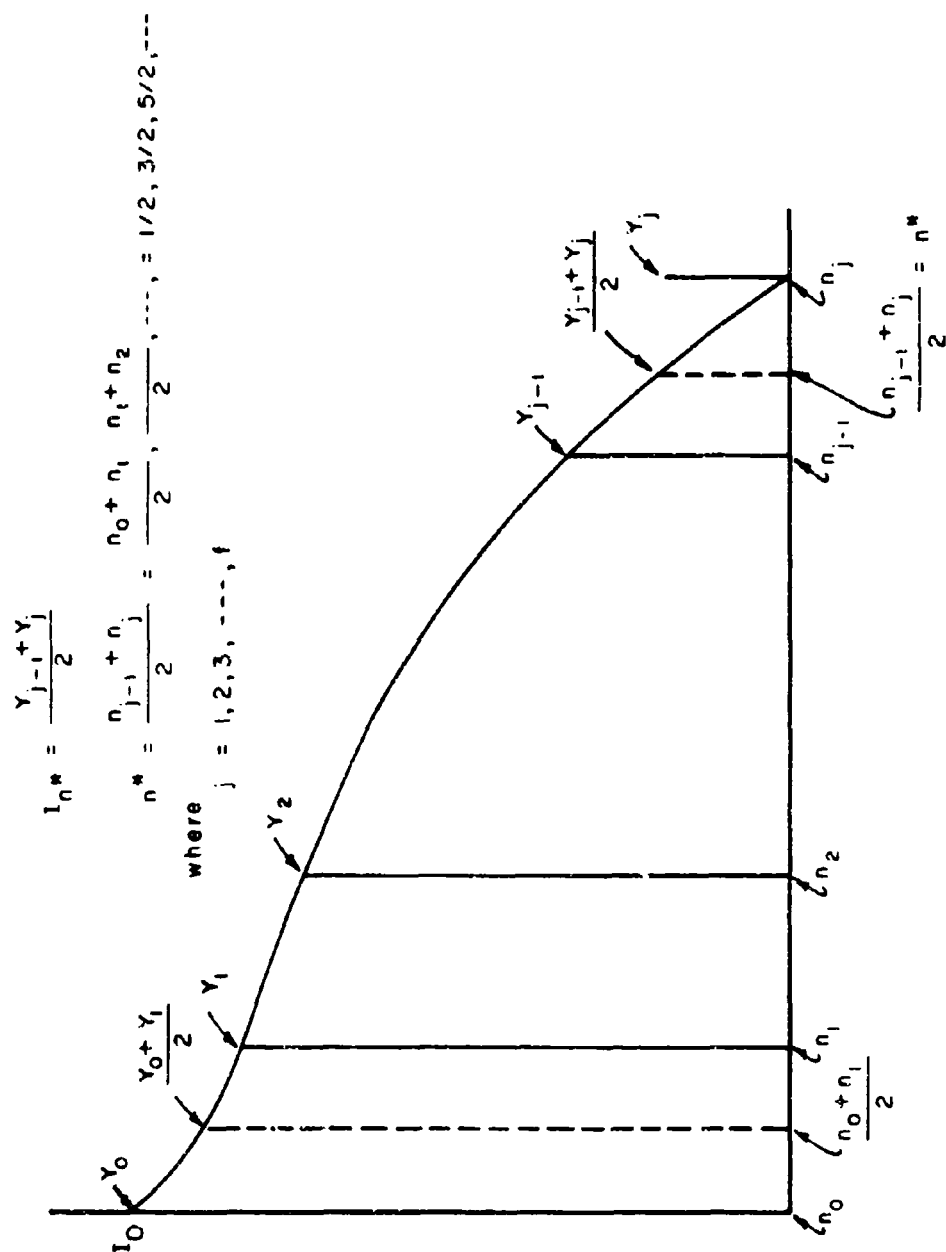


Figure 5. TOF Trace

If the beam is assumed to be isotropic in relation to specific charge distribution and mass flow distribution, by the derivation in Reference (6) the thrust, specific impulse, and efficiency become

$$F = \sqrt{2V} \frac{I_0 \bar{c}^{1/2}}{\bar{c}} \eta_D^{1/2} \quad (20')$$

where the factor η_D (the isotropic divergence efficiency = $\frac{(1 + \cos\beta)^2}{4}$) (24) arises from the divergence of the beam.

$$I_{sp} = \frac{\sqrt{2V}}{g_0} \bar{c}^{1/2} \eta_D^{1/2} \quad (21')$$

$$\eta_F = \frac{F^2}{2MP_{IN}} = \eta_S \eta_D = \frac{(\bar{c}^{1/2})^2}{\bar{c}} \eta_D \quad (23')$$

The separability of η_S and η_D is a consequence of the assumption of isotropy. However, the worst case would be if the beam were confined to the surface of a cone. The two efficiency factors would again be separable, and the divergence efficiency would be

$$\eta_D = \cos^2\beta \quad (24')$$

From the TOF collector, \bar{t} and \bar{t}^2 may be determined. Then \bar{c} , $\bar{c}^{1/2}$, and $(\bar{c}^{1/2})^2$ may be calculated. These values are then used to calculate the performance characteristics of a colloid engine as given by Equations (20), (21), (22), and (23).

2. DETERMINATION OF \bar{t} AND \bar{t}^2 FROM TOF MEASUREMENTS

When a TOF measurement is recorded, the needle potential is shorted to ground, and an oscilloscope records the current decay as a function of time. A Polaroid camera attached to the scope records the TOF traces. The TOF trace may be divided into incremental segments along the time axis as shown in Figure 5.

Equations (18) and (19) then may be expanded as follows:

$$\overline{t^2} = 2 \int_0^t \frac{I}{I_0} I dt \approx \sum_{n^*=1/2}^f \frac{2n^*(\Delta t)^2}{I_0} I_{n^*} \quad (25)$$

where

$$\Delta t = \Delta x, I_{n^*} = \frac{Y_{j-1} + Y_j}{2}, n^* = \frac{n_{j-1} + n_j}{2}$$

and scale conversion factors are

$$\ell = \mu \text{ sec/cm}, k = \mu \text{ amps/cm}$$

$$\begin{aligned} \overline{t^2} &= \frac{2(\Delta x)^2 \ell^2 k}{I_0} \sum_{j=1}^f \left[\left(\frac{n_{j-1} + n_j}{2} \right) \left(\frac{Y_{j-1} + Y_j}{2} \right) \right] \\ \overline{t^2} &= \frac{2(\Delta x)^2 \ell^2 k}{I_0} \left[\frac{1}{2} \left(\frac{Y_0 + Y_1}{2} \right) + \frac{3}{2} \left(\frac{Y_1 + Y_2}{2} \right) + \frac{5}{2} \left(\frac{Y_2 + Y_3}{2} \right) + \dots \right. \\ &\quad \left. + \left(\frac{N_{j-1} + N_j}{2} \right) \left(\frac{Y_{j-1} + Y_j}{2} \right) \right] \\ \overline{t^2} &= \frac{2(\Delta x)^2 \ell^2 k}{I_0} \left[\sum_{N=1}^{N_T} \frac{Y_0}{4} + Y_1 + 2Y_2 + 3Y_3 + \dots + NY_N \right] \\ \overline{t^2} &= \frac{2(\Delta x)^2 \ell^2 k}{I_0} \left[\frac{Y_0}{4} + \sum_{N=1}^{N_T} NY_N \right] \end{aligned} \quad (26)$$

In like manner, where N_T = total number of Δt 's chosen for calculation,

$$\bar{t} = \int_0^t \frac{I dt}{I_0} \approx \sum_{n^*=1/2}^f \frac{I_{n^*} \Delta t}{I_0} \quad (27)$$

$$\begin{aligned} \bar{r} &= \frac{\Delta x k L}{I_0} \sum_{j=1}^I \left[\frac{Y_{j-1} + Y_j}{2} \right] = \frac{\Delta x k L}{I_0} \left[\frac{Y_0 + Y_1}{2} + \frac{Y_1 + Y_2}{2} + \frac{Y_2 + Y_3}{2} + \dots \right. \\ &\quad \left. + \frac{Y_{j-1} + Y_j}{2} \right] \\ \bar{r} &= \frac{\Delta x k L}{I_0} \left[\frac{Y_0}{2} + Y_1 + Y_2 + Y_3 + \dots + Y_N \right] \\ \bar{r} &= \frac{\Delta x k L}{I_0} \left[\frac{Y_0}{2} + \sum_{N=1}^{N_T} Y_N \right] \end{aligned} \quad (28)$$

3. ASSUMPTIONS MADE FOR CONVENTIONAL CALCULATION OF ENGINE PARAMETERS

The procedures and equations just presented have been used by the electric propulsion industry to determine diagnostic performance of colloid engines composed of single-needle arrays and multi-needle arrays. In determining specific charge, thrust, specific impulse, and efficiency, however, the following assumptions were made by the industry.

- a. Charged particles are accelerated to their final velocities in a very small distance compared to the TOF collector distance.
- b. All charged particles fall through the same acceleration potential. The energy required to form the charged droplets is small compared to the fraction of the total applied potential. Therefore, almost all of the applied voltage goes into accelerating the charged particles.
- c. The beam is isotropic in regard to specific charge distribution and mass flow distribution over some finite cone of half angle β .

Assumption (b) has been challenged by Burson (Reference 3). He has found that the velocity distribution is due not only to specific charge distribution, but, to some degree, to a voltage distribution caused by losses during droplet

formation. He summarizes that the most reasonable loss mechanism at the needle tip is joule heating and conduction along the needle but that this has not been confirmed experimentally.

The author has investigated the validity of assumption (c) upon which Equations (20'), (21'), and (23') have been based. If the mass flow is not isotropic over some finite cone of half angle β , then these equations give incorrect values of thruster performance. The mass flow at some value of half angle β is given by

$$\dot{m}_\beta = \frac{I_\beta}{\bar{c}_\beta}$$

where I_β is the current to a collector situated at the half angle β , and \bar{c}_β is the specific charge determined from the current, I_β . If the mass flow is anisotropic with β , it can be due either to an anisotropic current distribution, a variance in \bar{c}_β determined from half angle to half angle, or both conditions. Figure 6 shows the possible conditions of mass flow and specific charge distribution with β .

The following describes the techniques used and the equations derived to determine the colloid engine performance calculations based on anisotropic conditions within the beam. If all conditions are isotropic, the equations still apply.

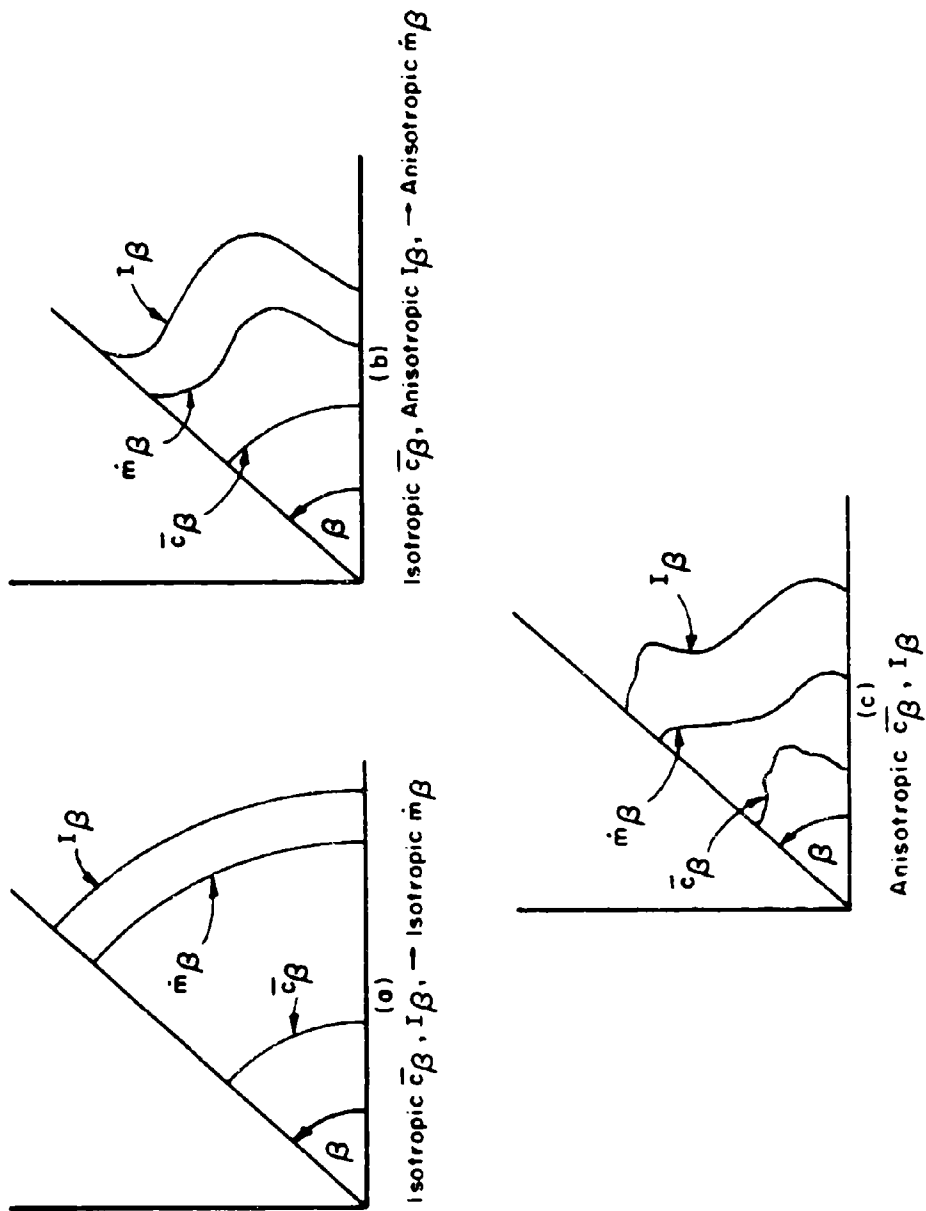


Figure 6. Possible Current, Specific Charge, and Propellant Mass Flow Distributions

SECTION V

DETERMINATION OF THRUSTOR PERFORMANCE
CHARACTERISTICS BASED ON ANISOTROPIC CONDITIONS

To determine how m varies in the beam, it is necessary to determine the value of $\bar{c}_{\beta\alpha}$ and $I_{\beta\alpha}$ at individual points within the beam, and then to perform a summation of these data points to determine \bar{c} (the average for the entire beam), η , and I_{sp} .

The following equations are derived:

For each data point, the thrust component of a section of the beam in the x -direction is

$$f_{\beta\alpha_x} = \dot{m}_{\beta\alpha} \bar{v}_{\beta\alpha} \sin \theta \cos \phi \quad (29)$$

The subscript $\beta\alpha$ indicates, as shown in Figure 7, each individual data point, e.g., for each value of β from 0° to 70° , α varies in incremental degrees from 0° to 360° . From Figure 7, $\sin \theta \cos \phi = \cos \beta$; and

$$\dot{m}_{\beta\alpha} = \frac{I_{\beta\alpha}}{\bar{c}_{\beta\alpha}}, \quad \bar{v}_{\beta\alpha} = \sqrt{2V} \bar{c}_{\beta\alpha}^{1/2}$$

where $\bar{c}_{\beta\alpha}$, $\bar{c}_{\beta\alpha}^{1/2}$ are given by Equation (10') and (12')

$$\therefore f_{\beta\alpha_x} = \frac{I_{\beta\alpha}}{\bar{c}_{\beta\alpha}} \sqrt{2V} \bar{c}_{\beta\alpha}^{1/2} \cos \beta$$

Therefore, the total thrust in the x -direction contributed by the beam is

$$F_x = \sum_{\beta\alpha} f_{\beta\alpha_x} = \sqrt{2V} \sum_{\beta\alpha} \frac{I_{\beta\alpha}}{\bar{c}_{\beta\alpha}} \bar{c}_{\beta\alpha}^{1/2} \cos \beta \quad (30)$$

Power in the beam is

$$P_{IN} = V \sum_{\beta\alpha} I_{\beta\alpha} \quad (31)$$

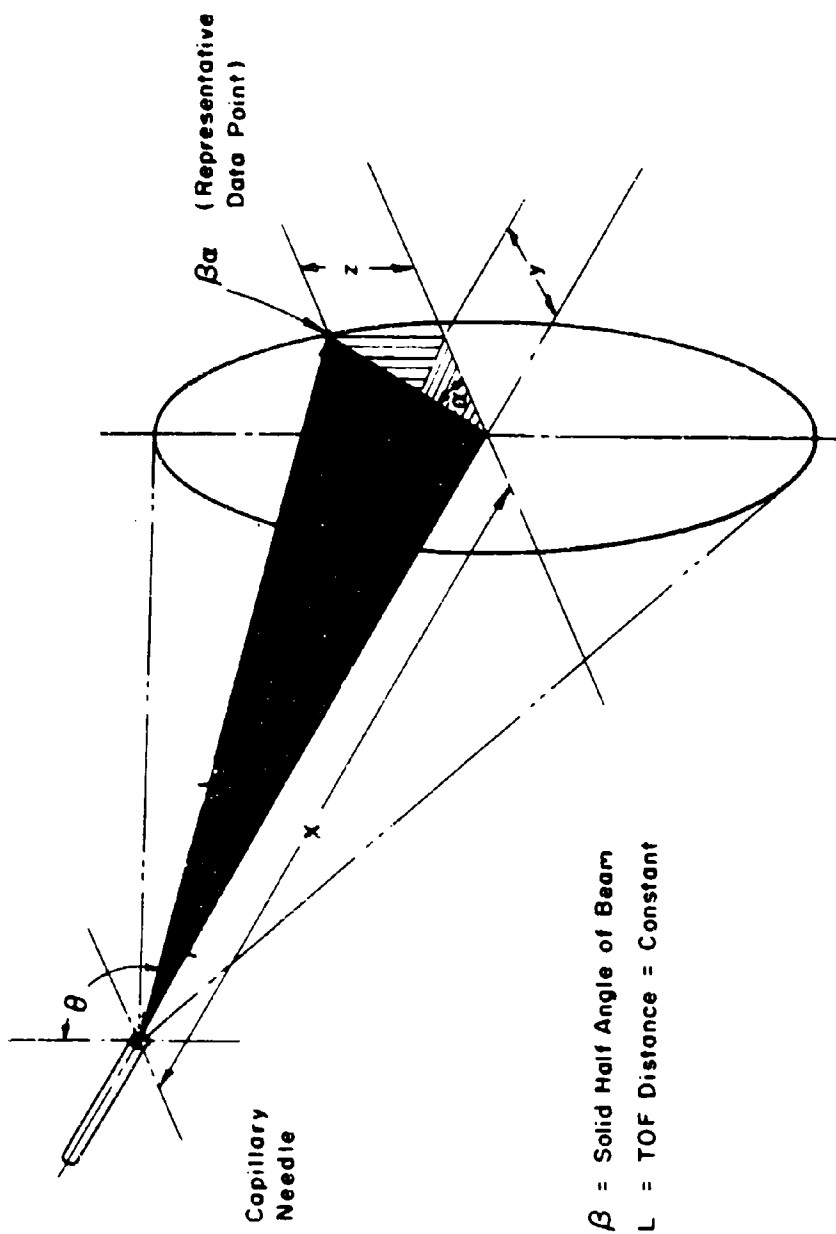


Figure 7. Geometry of Source Collector

and total propellant mass flow is

$$\dot{M} = \sum_{\beta\alpha} \dot{m}_{\beta\alpha} = \sum_{\beta\alpha} \frac{I_{\beta\alpha}}{\bar{c}_{\beta\alpha}} = \frac{I}{\bar{c}} \quad (32)$$

Therefore, thrust efficiency due to specific charge distribution and beam divergence is

$$\eta_F = \frac{F_x^2}{2 \dot{M} P_{IN}} = \frac{2V \left[\sum_{\beta\alpha} \frac{I_{\beta\alpha}}{\bar{c}_{\beta\alpha}} \frac{1}{\bar{c}_{\beta\alpha}^{1/2}} \cos \beta \right]^2}{2 \left[\sum_{\beta\alpha} \left(\frac{I_{\beta\alpha}}{\bar{c}_{\beta\alpha}} \right) \right] \left[V \sum_{\beta\alpha} I_{\beta\alpha} \right]} \quad (33)$$

Specific impulse is given by

$$I_{sp} = \frac{F_x}{\dot{M} g_0} = \frac{\sqrt{2V} \sum_{\beta\alpha} \left(\frac{I_{\beta\alpha}}{\bar{c}_{\beta\alpha}} \frac{1}{\bar{c}_{\beta\alpha}^{1/2}} \cos \beta \right)}{\sum_{\beta\alpha} \frac{I_{\beta\alpha}}{\bar{c}_{\beta\alpha}} g_0} \quad (34)$$

and the mass-weighted average value of specific charge is

$$\bar{c} = \frac{\sum_{\beta\alpha} I_{\beta\alpha}}{\sum_{\beta\alpha} \dot{m}_{\beta\alpha}} = \frac{I}{\dot{M}} = \frac{\sum_{\beta\alpha} I_{\beta\alpha}}{\sum_{\beta\alpha} \frac{I_{\beta\alpha}}{\bar{c}_{\beta\alpha}}} = \frac{(I_{\beta\alpha})_1 + (I_{\beta\alpha})_2 + \dots}{\frac{(I_{\beta\alpha})_1}{(\bar{c}_{\beta\alpha})_1} + \frac{(I_{\beta\alpha})_2}{(\bar{c}_{\beta\alpha})_2} + \dots} \quad (35)$$

also,

$$\frac{1}{\bar{c}^{1/2}} = \frac{\sum_{\beta\alpha} \dot{m}_{\beta\alpha} \frac{1}{\bar{c}_{\beta\alpha}^{1/2}}}{\sum_{\beta\alpha} \dot{m}_{\beta\alpha}} = \frac{F \text{ (calculated for non-divergent beam)}}{\sqrt{2V} \dot{M}} \quad (35')$$

The anisotropic thrust determination (Equation 30) is simply a summation of Equation (20') for $\eta_D = \cos^2 \beta$, the case where the beam is confined to the surface of a cone. Also, for small values of β ,

$$\frac{1 + \cos \beta}{2} \rightarrow \cos \beta$$

the isotropic determination of thrust approaches the hollow cone determination.

In other words, if β is small, Equation (20') with $\eta_D^{1/2} = \sqrt{\frac{(1 + \cos \beta)^2}{4}}$ can be summed at each TOF data point to arrive at approximately the same results as those obtainable from Equation 30. If the beam is confined to a hollow cone at some value of β , Equation (20') with $\eta_D = \cos^2 \beta$ can be summed at each TOF data point to arrive at the same results as those obtained from Equation (30).

SECTION VI

EXPERIMENTAL SETUP AND PROCEDURES

Since the experimental plan was to observe small segments of the beam and sum the results to determine an average \bar{c} and $\bar{c}^{-1/2}$, for the entire beam, a TOF collector had to be designed. Three different design approaches were considered.

1. SEGMENTED HEMISPHERICAL COLLECTOR

A TOF collector (Figure 8a) in the form of a hemisphere insulated so that incremental currents could be measured was considered as a possible approach to mapping the beam. This approach had the advantage of collecting almost the entire beam. Also, no movable parts were included. However, the fabrication of individual "patches" on the inner surface to collect the incremental currents appeared to be a formidable task. The electrical circuitry, including leads from each "patch" collector, and the switching panel connecting the collector to the oscilloscope appeared too cumbersome and complex. This approach was dropped.

2. BOOM COLLECTOR

A TOF collector in the form of a small spherical collector attached to the end of a boom (Figure 8b) was considered. On the surface, this seemed a good approach. The small collector could be moved in and out and in a circular arc, pivoting about the flexible metal vacuum fitting. However, knowing the precise location of the ball collector was another matter. A pointer at the opposite end of the boom could locate a position on a movable plate. With a fixed distance x of the plate from the vacuum flange, the ball could be rotated in a circular arc of radius a_1 through the beam. By moving the boom in or out, a larger or smaller circle of radius a_2 could be mapped. Figure 9 shows the position of the plate as a function of x and z for various half angles, β . As can be seen, many of the rings on the plate are close to each other, making the pointer very difficult to position. In addition, as β is changed, x changes, and therefore, the TOF distance varies. This makes the summation computations more difficult. Because of the difficulties this approach was not tried.

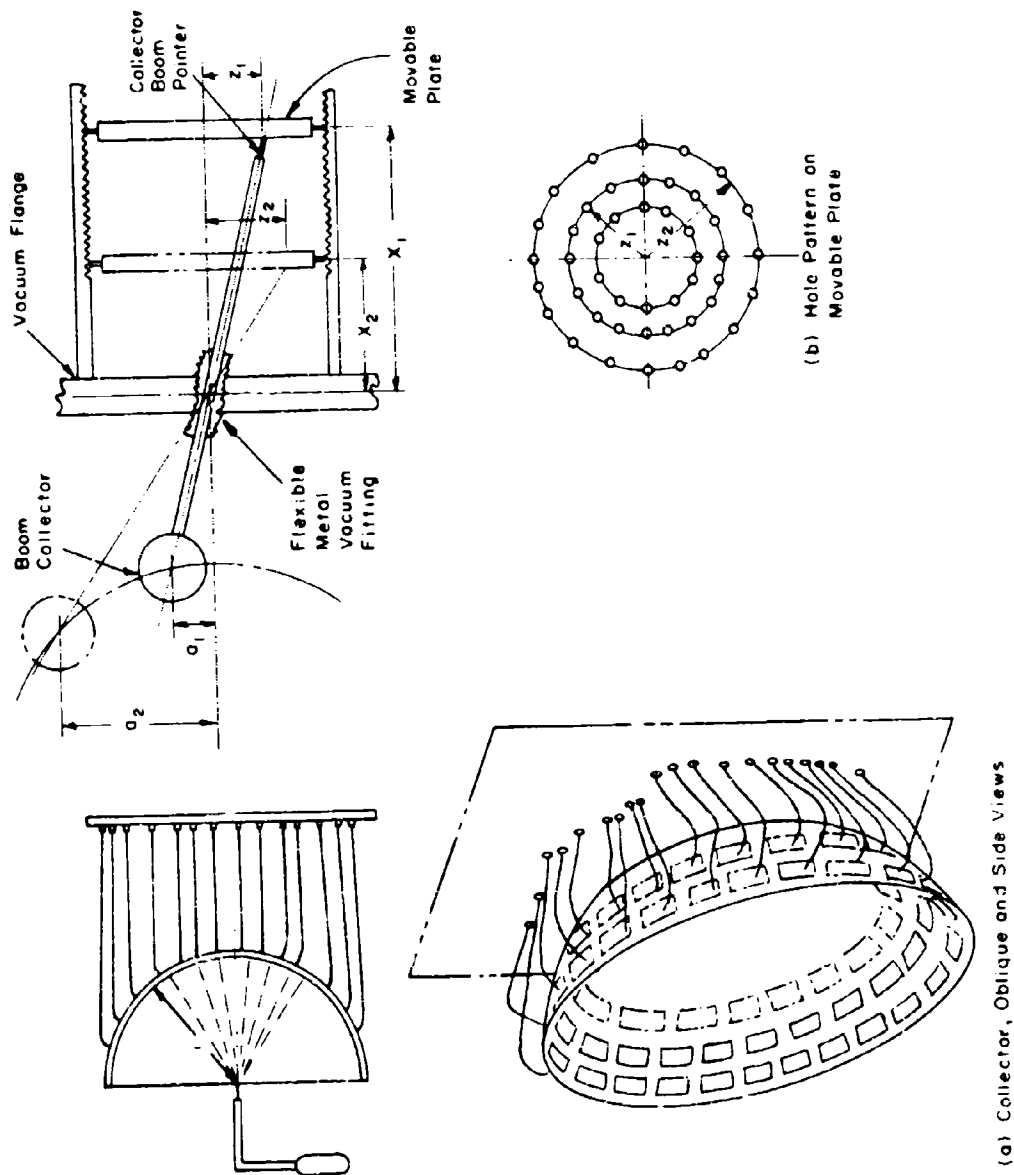


Figure 8. Possible IOF Collector Designs

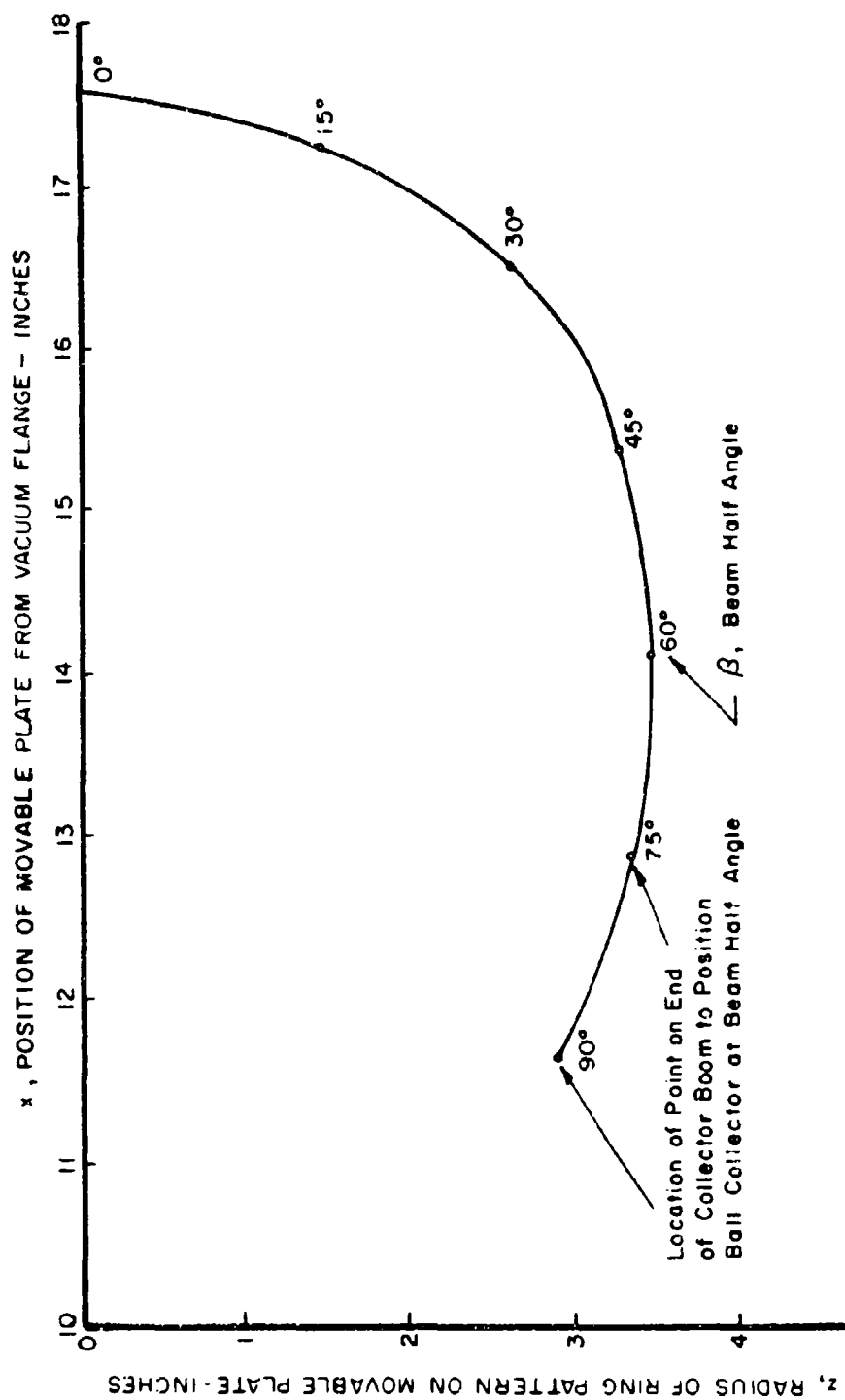


Figure 9. Positions of Collector Boom Pointer and Movable Plate for Locating Boom Collector

3. GEARED BALL CURRENT COLLECTOR (BC)

The third design approach was to position a small (9/16" dia.) stainless steel ball on the end of a gear rack and pinion. The rack and pinion were fastened to the outside of a 3/4" stainless steel tube about 21" in length. Inside the tube, running along the axis of the tube, was a 1/4" rod which was attached to the pinion. Figure 10 shows the assembly. By turning the rod, the pinion rotated and raised or lowered the ball on the end of the rack. In addition to this movement, the mechanism could be rotated about the axis passing through the hollow tube by turning a collector support brace attached to the tube (Figure 11). The ball collector, therefore, could be rotated about the colloid needle axis a full 360°, azimuthally at various radii depending on how far the rack was moved.

In addition to the preceding movements, another important movement could be made. By turning a threaded rod which passes through a larger (collector control rod brace) brace attached to the vacuum flange and then passing freely through the collector support brace, the entire mechanism could be moved along the axis, inward or outward, about 5 inches.

With this arrangement, it was possible to keep a fixed distance L (TOF distance) from the needles and position the ball collector at any location in the beam.

Thus, for each half angle of $\beta_1 = 0, \beta_2, \beta_3 \dots \beta = 70^\circ$, the ball collector could map the beam at azimuthal angles of $\alpha_1 = 0, \alpha_2, \alpha_3 \dots \alpha = 360^\circ$, at a constant TOF distance (Figure 7). The ball collector, therefore, could map over the surface of a sphere L inches away from the engine. If a different TOF distance was desired, this could easily be changed, and the collector again could be mapped over a spherical surface.

4. TOTAL CURRENT COLLECTOR (TC)

In addition to the movable ball collector, a hemispherical collector of 1 3/4" radius was designed and fabricated. When mounted on a rod extending from the colloid engine vacuum flange, the total current collector could be



Figure 10. Geared Ball Current Collector (BC) Assembly

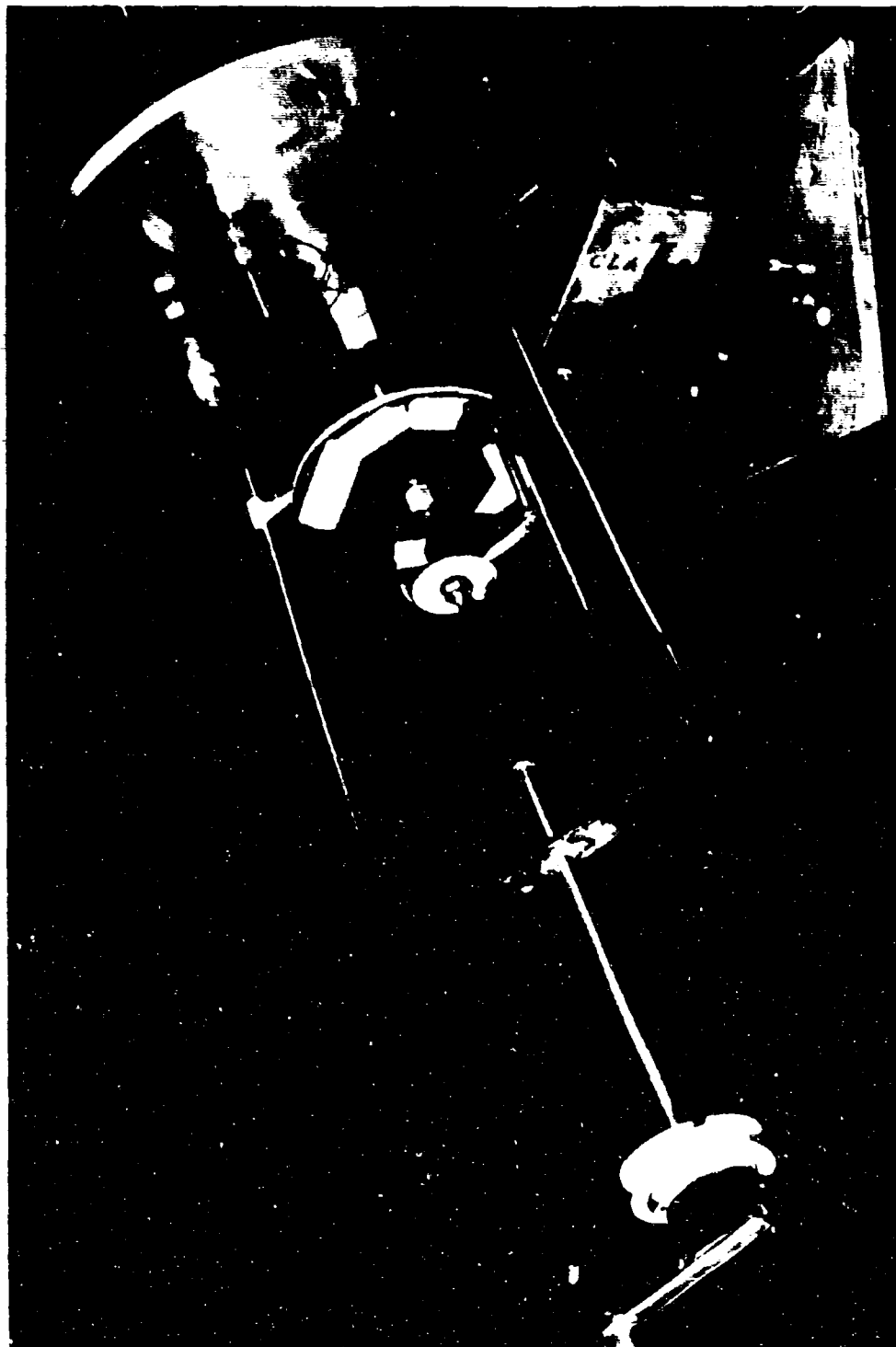


Figure 11. Controls for Positioning Geared Ball Current Collector Assembly

extended outward from the flange and rotated to a position directly in front of the engine for a total current TOF trace. Then this could be compared with the summation ball collector (BC) TOF traces. Figure 12 shows the colloid engine TC collector arrangement, while Figure 13 shows the mechanical arrangement on the back of the colloid engine flange (upper portion of flange) for extending and rotating the TC collector. The transparent plastic rod shown is for rotating the collector to a position in front of the engine.

5. COLLOID SOURCE

A single needle and a three-needle array were used in the diagnostic program. The single-needle engine had a stainless steel needle of 0.008" O.D., 0.004" I.D. x 4 cm. The needle, during normal operation, was positioned in the aperture of the extractor electrode along the electrode axis, and in the plane of the grid. A mechanical arrangement could move the extractor electrode slightly forward and backward so that the effects of the extractor positioning on the beam shape could be determined. However, for this study, the needles were positioned flush with the front surface of the extractor. Figure 13 shows the mechanical setup for (center of flange) positioning the extractor. The extractor electrode was made of 1/16" stainless steel with a 7/32" diameter aperture with rounded edges. The 3-needle array was obtained under contract. The platinum needles are 0.014" O.D. and 0.004" I.D. with a 10° funnel level at the emitting end.

The propellant selected for the tests had a mixture ratio of 15 grams of NAI to 100 ml of glycerol. The purpose of the sodium iodide is to produce an ionically conducting liquid which is amenable to charging during the spraying process (Reference 7). This propellant is used widely throughout the electric propulsion industry because of its high degree of solubility. Glycerol is used because it has a low vapor pressure and is a good solvent for many ion-forming salts. A low vapor pressure is desirable to minimize the loss of propellant mass by evaporation during particle formation and acceleration (Reference 8).

The propellant feed system consists of a fluid reservoir connected to a manometer and a liquid nitrogen pressure bottle. Feed flow rate is controlled by a bleed valve and the required pressure is read on the manometer.



Figure 12. Single-Needle Source and Movable Total Current Collector (TC) Assembly

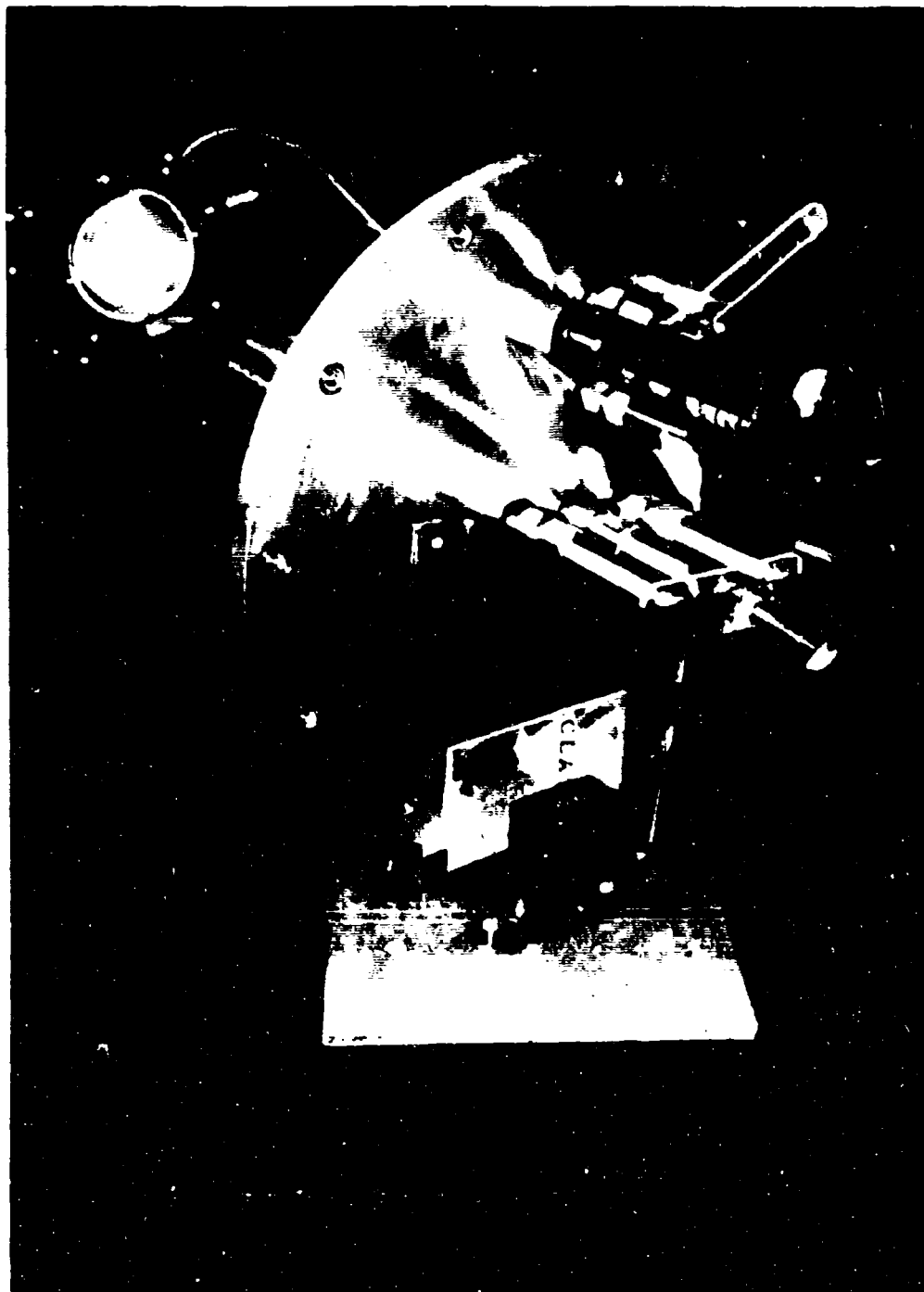


Figure 13. Controls for Moving Total Current Collector Assembly and for Positioning Extractor

The geometrical arrangement of a single-needle engine and the TC and BC collectors is shown inside the vacuum chamber in Figure 14. A screen can be seen around the sides of the needle. This screen, which is electrically connected to the extractor and at the same potential, provides a barrier preventing electrons in the chamber environment from going to the positively charged needle. The screen around the BC collector can be seen and is charged negative with respect to the collector to suppress secondary electrons that are emitted as the charged droplets strike the collector.

6. VACUUM CHAMBER AND TOF SCOPE SYSTEMS

The vacuum chamber consisted of a 12" diameter glass tee and a 6" CVC vacuum pumping system with a LN_2 cold trap. A reducing flange mated the 12" tee with the 6" diffusion pumps. Pressures on the low 10^{-6} Torr scale were recorded during engine operation.

A Tektronix, Inc. Model 355 memory scope, mounted in a movable power supply rack, was used to record the TOF traces. The scope, which was connected to the TOF collector, was triggered by a thyatron discharge circuit as it pulsed the capillary potential to ground. A Polaroid camera attached to the scope recorded the traces.

Figure 15 shows the entire colloid engine diagnostic setup.

On the left is the positive and negative high voltage power supplies, the oscilloscope/camera, and the necessary voltmeters and ammeters. Through the spherical part of the tee can be seen the colloid needle and extractor. The box resting on the vacuum system controls the scope resistances and plugs into the scope and either one of the TOF collectors. The electrical schematic for the entire setup is shown in Figure 16.



Figure 14. View of Single Needle Colloid Source, Total Current Collector, and Ball Current Collector, Inside Vacuum Chamber



Figure 15. Colloid Source Diagnostic Setup

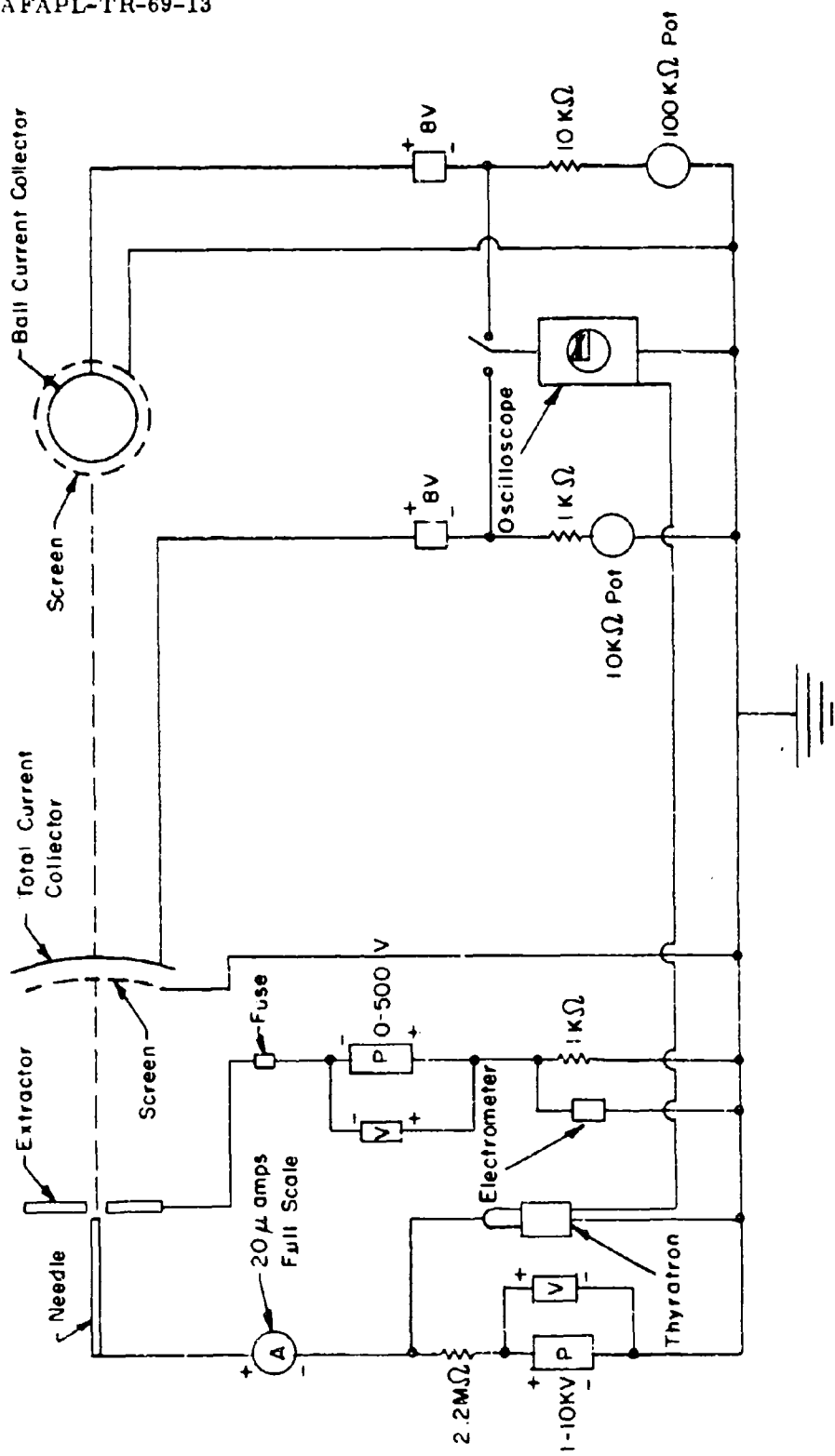


Figure 16. Colloid Source TOF Collector Electrical Schematic

SECTION VII

RESULTS OF DIAGNOSTIC TESTS

The first experimental setup employed a single-needle colloid source, while the last two used the three-needle array. Table I lists the conditions under which the tests were made.

TABLE I
OPERATING CONDITIONS FOR COLLOID DIAGNOSTIC EXPERIMENTS

Conditions Common to Each Test	TEST I (Single Needle)	TEST II (Three-Needle Array)	TEST III (Three Needle Array)
Source Material and Geometry (OD x ID) mils	Stainless Steel 8 x 4	Platinum 14 x 4 With 10° Funnel Level	Platinum 14 x 4 With 10° Funnel Level
Propellant (grams NaI/ml glycerol)	15 / 100	15 / 100	15 / 100
Propellant Resistivity ($K\Omega$ -cm at 30°)	2.95	2.9	2.9
Needle Voltage (volts)	2500	5300	4800
Extractor Voltage (volts)	-450	-450	-485
Vacuum Pressure (Torr)	1.6×10^{-6}	3.3×10^{-6}	3×10^{-6}
Feed System Pressure (Torr)	2.5	2.0	2.8
Source Current (μ amperes)	3×10^{-6}	12×10^{-6}	6×10^{-6}

Because of the great bulk of data that had to be reduced and plotted, only Test No. II is reported in detail, although ample data is available for determining more performance results for Test I and III.

A digital computer program was developed and used in most of the data reductions and calculations, because of the great volume of data that needed to be reduced. The program is shown in the appendix.

1. TAKING THE DATA

A single TOF was recorded on the total current collector (TC) while many traces were recorded on the ball current collector (BC). In taking the BC data, a value of β was first selected (Figure 7). Then the ball collector was rotated an incremental $\Delta\alpha$ and a TOF trace was taken.

This procedure was then followed through equal incremental $\Delta\alpha$'s over the entire 360° . The BC was then positioned at another value of β , and the entire procedure was repeated. TOF traces were taken at incremental values of $\Delta\alpha = 20^\circ$, at the values of β greater than 25° , and at slightly larger values of $\Delta\alpha$ at smaller values of β . This was done to prevent overlapping of TOF readings and to reduce the number of TOF traces that had to be reduced. Current readings, however, were taken at incremental values of $\Delta\alpha = 5^\circ$. On all three tests, approximately 500 current readings were recorded; about 270 TOF traces were made with 135 photographed. Of these, about 90 TOF traces were inspected, and the data was reduced for performance calculations.

A sample BC TOF trace is shown in Figure 17 for the single-needle Test No. 1 for $\beta = 25^\circ$, $\alpha = 150^\circ$.

The horizontal scale is 10 microseconds/cm and the vertical scale is 1 millivolt/cm = 1.01×10^{-8} amperes/cm. Needle voltage was 2500 volts with 3μ amperes needle current recorded at the ammeter. The charge-to-mass ratio determined for this data point was $\bar{c} = 170.95$ coul/kg.

2. TEST II (THREE-NEEDLE ARRAY)

Figure 18 shows the TOF trace on the TC for the three-needle array (Test II). While Figure 19 shows a typical TOF trace on the BC at $\beta = 25^\circ$, $\alpha = 30^\circ$. The vertical scale of the TC is 10 millivolts/cm (0.92×10^{-6} amperes/cm), while that for the BC is 2 millivolts/cm (2.02×10^{-8} amperes/cm). TOF distance was 1.95" for the TC and 5" for the BC. TOF determinations were $\bar{c} = 24.2$ coul/kg for the TC and $\bar{c}_{\beta\alpha} = 66.6$ coul/kg for this particular ball collector position.

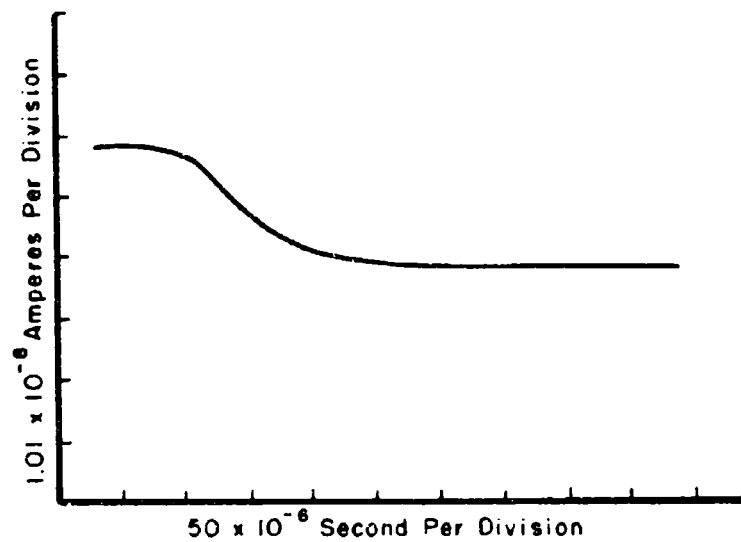


Figure 17. Single-Needle Ball Current Collector (BC) TOF Trace:
 $L = 5''$, $\beta = 25^\circ$, $\alpha = 150^\circ$, $\bar{c}_{\beta\alpha} = 171$ Coulombs/Kg

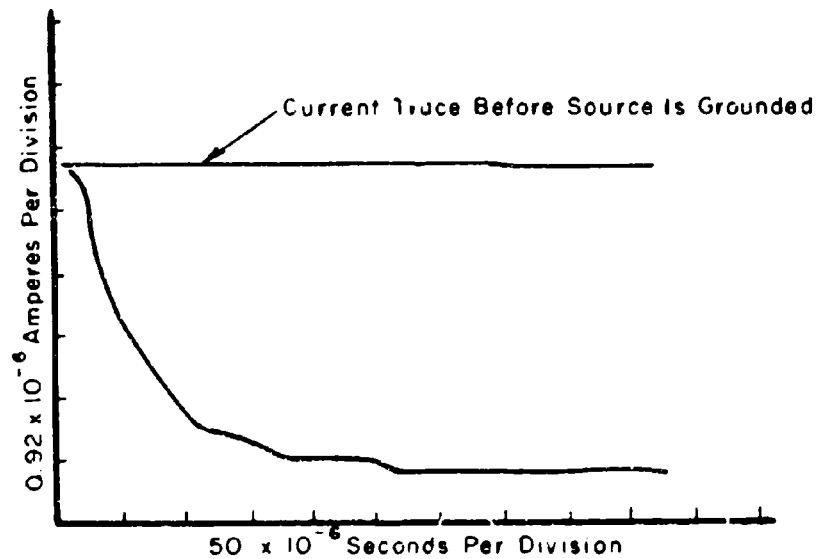


Figure 18. Three-Needle Array Total Current (TC) TOF Trace:
 $L = 1.95''$, $\bar{c} = 24.2$ Coulombs/Kg

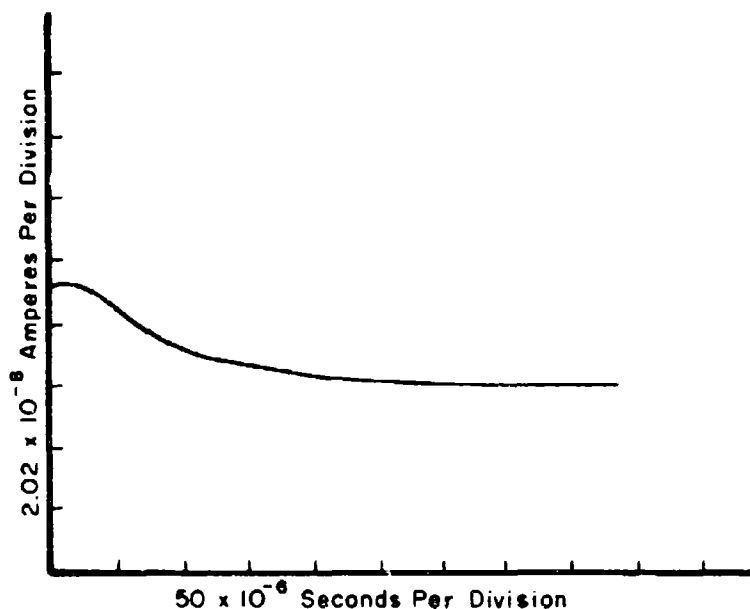


Figure 19. Three-Needle Array Ball Current Collector (BC)
 TOF Trace: $L = 5''$, $\beta = 25^\circ$, $\alpha = 30^\circ$, $\bar{c}\beta\alpha = 66.6$
 Coulombs/Kg, $\bar{c} = 63.8$ Coulombs/Kg

a. Determination of Current and Mass Flow Distribution and Total Mass Flow Rate

While many current and TOF data points were taken as a function of β and α , it is obvious that a large fraction of the beam was not sampled by the ball collector, as shown in Figure 20. It was necessary, therefore, to plot the available data points and perform a graphical integration to obtain the correct values of current and mass flow. This procedure was as follows.

Figure 21 shows the beam current measured at the ball collector for a given value of $\beta = 25^\circ$ as a function of α ($\Delta\alpha = 5^\circ$).

Figure 22 shows the TOF charge-to-mass calculation for $\beta = 25^\circ$, as a function of α . These points were determined for incremental $\Delta\alpha = 20^\circ$. Straight lines were connected to each data point. The resultant propellant mass flow measured at the ball collector is shown in Figure 23 for $\beta = 25^\circ$, as a function

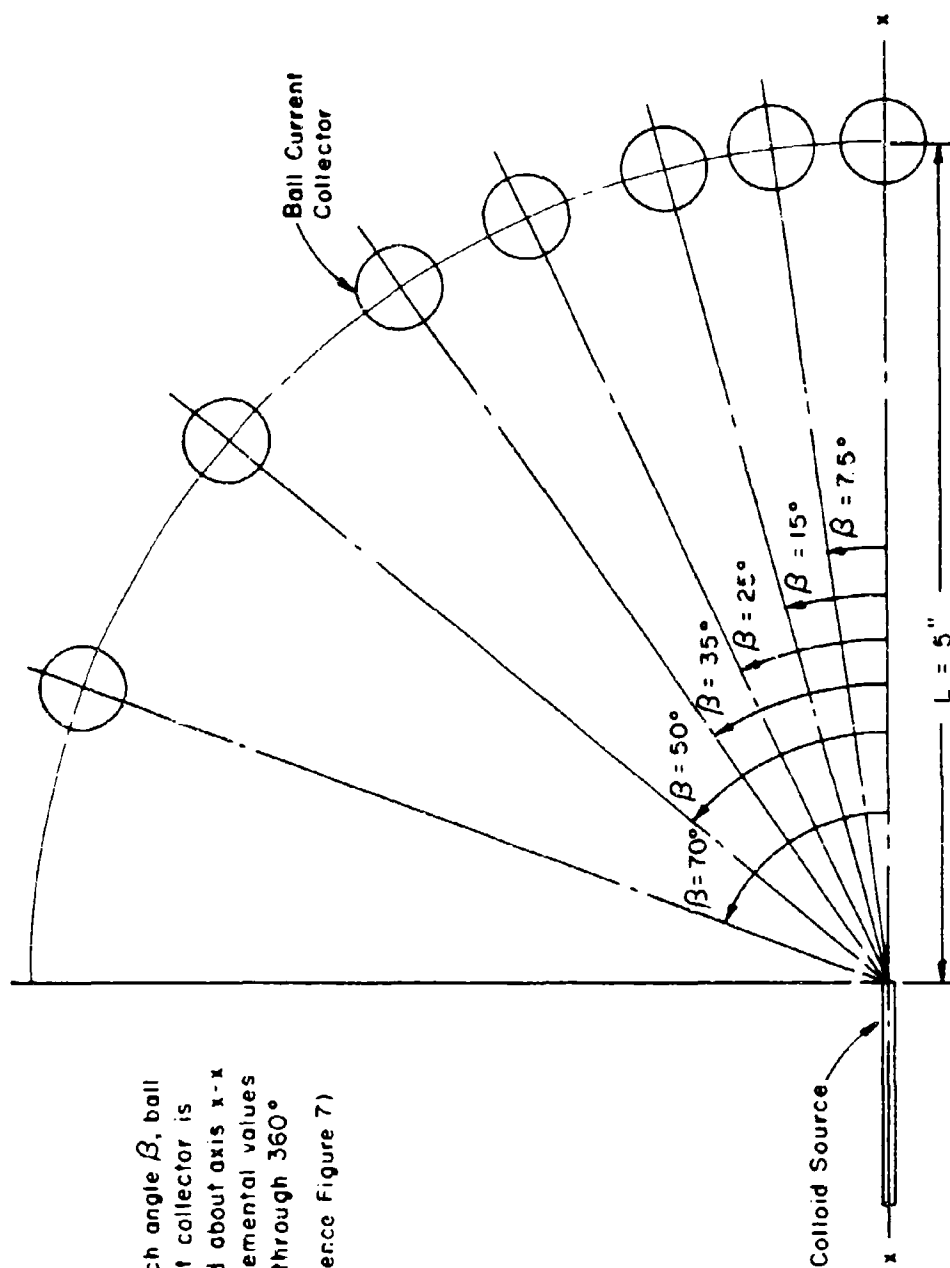


Figure 20. Various Positions of Ball Current Collector for Taking Data

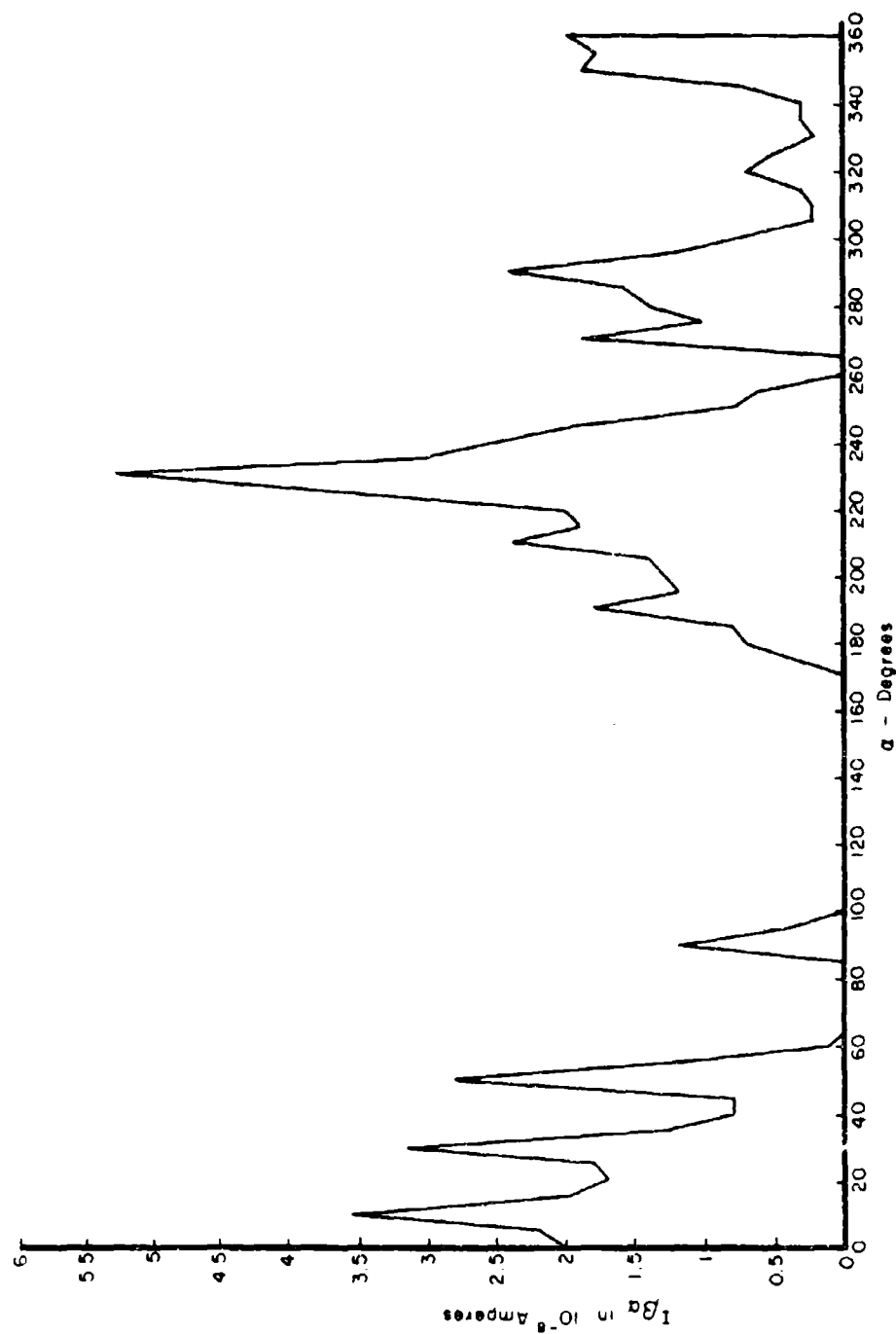


Figure 21. Beam Current Measured at Ball Current Collector as a Function of Azimuthal Angle, α , for $\beta = 25^\circ$

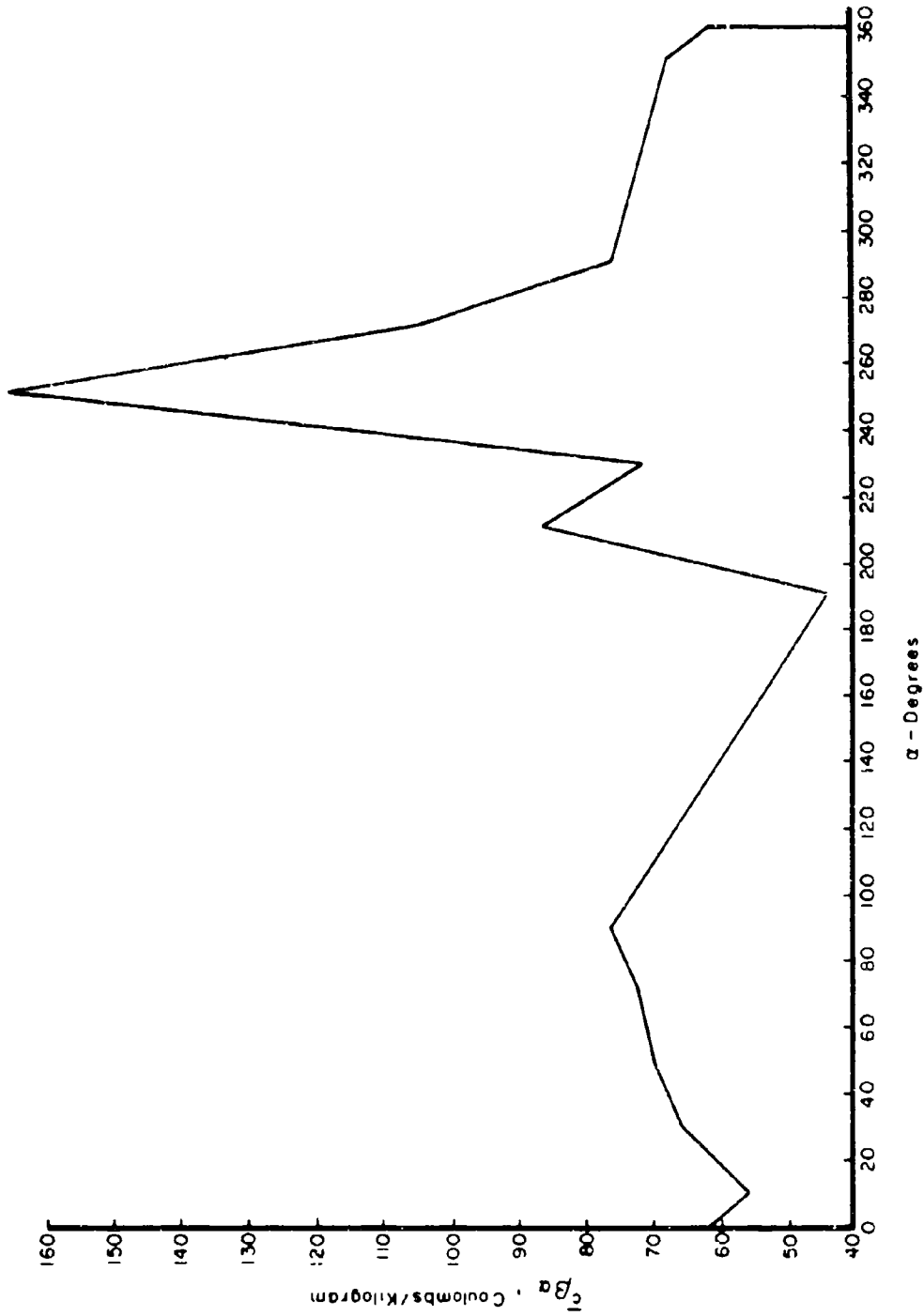


Figure 22. Specific Charge, Determined from Ball Collector TOF Traces, as a Function of Azimuthal Angle α for $\beta = 25^\circ$

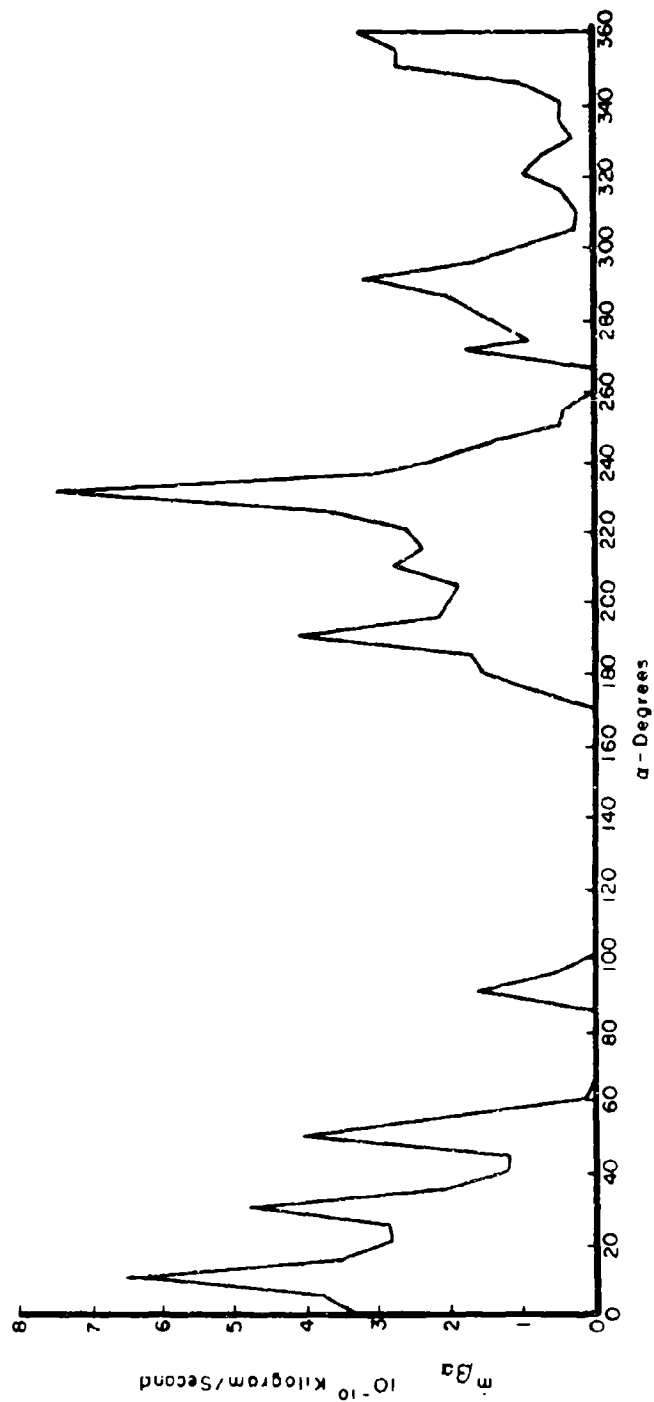


Figure 23. Propellant Mass Flow, Calculated at the Ball Collector as a Function of Azimuthal Angle, α for $\beta = 25^\circ$

of α ($\Delta\alpha = 5^\circ$). The average mass flow density measured by the ball collector as a function of the angle β is then determined as follows:

$$\bar{m}_{\rho\beta} = \frac{1}{2\pi} \sum_{\alpha} \frac{\dot{m}_{\beta\alpha}}{a} \Delta\alpha, \text{ in kg/sec-in}^2 \quad (\text{Ref 9}) \quad (36)$$

where

a = cross-sectional area of ball collector = 0.25 in^2 .

$\dot{m}_{\beta\alpha}$ = mass flow measured at ball collector in kg/sec = $\frac{I_{\beta\alpha}}{c_{\beta\alpha}}$ at each point.

The average mass flow density at a given position in the beam was determined by weighting the $\dot{m}_{\beta\alpha}$ vs α graph. Using the information that the graph paper weight 0.06 grams/in^2 , and the size of the graph was $9'' \times 6''$, the weight of the graph paper is determined to be $54 \times 0.06 \text{ grams} = 3.25 \text{ grams}$. Therefore, $3.25 \text{ grams} = 12 \times 10^{-10} \text{ kg/sec}$ (the value of the $6''$ ordinate scale) $\times 2\pi$ radians (the value of the $9''$ abscissa scale) $\therefore 1 = 23.25 \times 10^{-10} \text{ kg-radians/gram-sec}$. Therefore,

$$\bar{m}_{\rho\beta} = \left(\frac{1}{2\pi \text{ radians}} \right) \left(\frac{1}{0.25 \text{ in}^2} \right) \left(\frac{23.25 \text{ kg-radians}}{\text{gram-sec}} \right) (\dot{m}_{\beta\alpha} \Delta\alpha \text{ grams})$$

where $\dot{m}_{\beta\alpha} \Delta\alpha$ is cut out and weighed on a Right-A-Weight balance scale.

This procedure was used for $\beta = 0^\circ, 7.5^\circ, 15^\circ, 25^\circ, 35^\circ, 50^\circ$, and 70° and then a smooth curve was drawn in Figure 24 for $\bar{m}_{\rho\beta}$ versus β . This curve now represents the mass flow density distribution as a function of β .

The mass flow distribution as a function of β and the total mass flow can now be calculated as follows:

$$\dot{M} = \sum_{\beta} \bar{m}_{\rho\beta} \Delta A = \sum_{\beta} \dot{m}_{\beta} \quad (37)$$

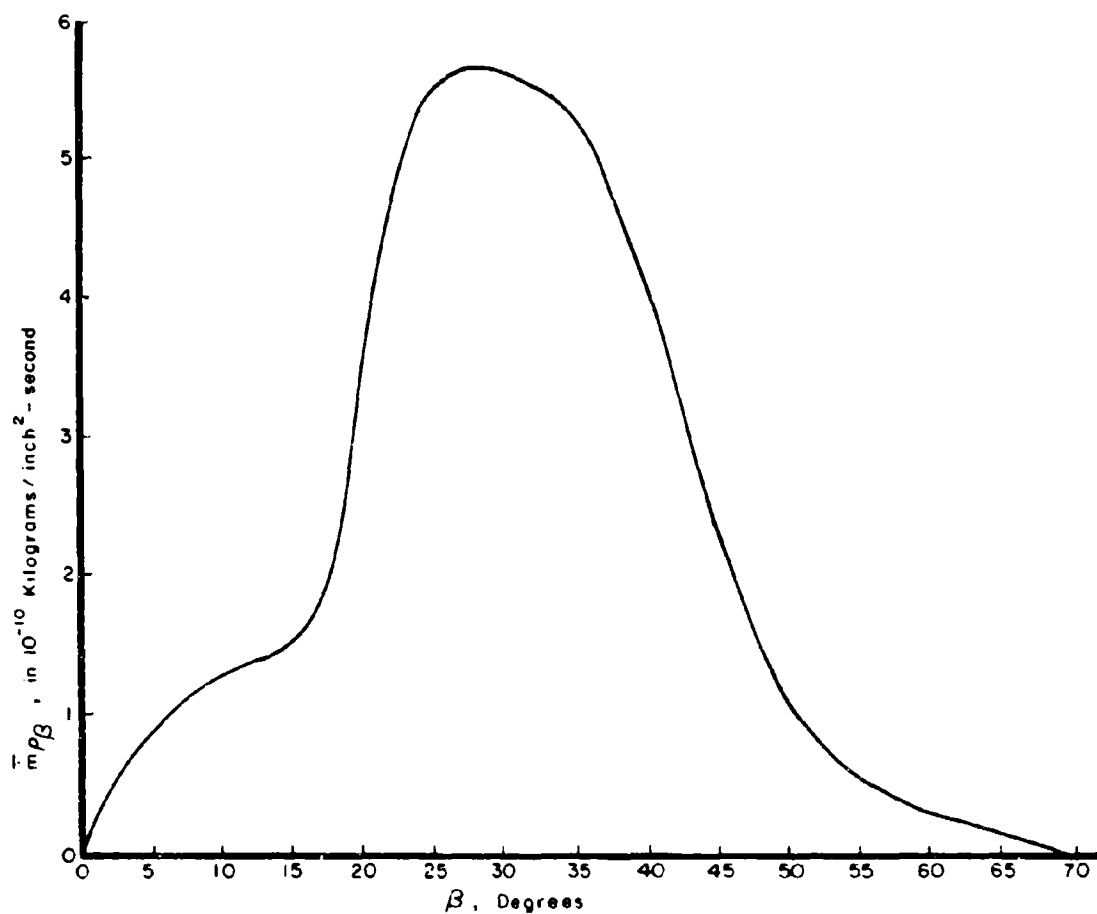


Figure 24. Propellant Mass Flow Density, Calculated at the Ball Collector, as a Function of Azimuthal Angle, α , for $\beta = 25^\circ$

where ΔA = approximate elemental surface area of circular strip of radius R , and width ΔS , at angle β (See Figure 25).

$$\therefore \dot{M} = \sum_{\beta} \bar{m}_{\rho\beta} 2\pi r^2 \sin \beta \Delta \beta, \text{ in kg/sec}$$

For the ball collector, the angle subtended by the ball was $\Delta \beta = 2.5^\circ = .044$ radians, and the distance of the needle to the ball collector was $r = 5''$.

$$\therefore \dot{M} = 6.84 \sum_{\beta} \bar{m}_{\rho\beta} \sin \beta, \text{ in kg/sec}$$

Total current measured for Test II by the above procedure was determined to be 1.4×10^{-6} amperes. Total mass flow determined graphically at each point and summed with the use of Equation (32) was 2.2×10^{-8} kg/sec. However, it will be shown later in Section VII, Paragraph 2b, that the current and mass flow must be corrected because interference of the ion beam with the extractor electrode and the collector screen reduces the percent of ions reaching the collector and causes secondary electrons to travel from the screen to the collector, further reducing the measured current reading. This however, will not change the mass flow distribution. The corrected mass flow and the mass flow distribution are shown as a function of half angle β in Figure 26 (See Section VII, Paragraph 2b(2), for corrected mass flow determination).

The average charge-to-mass ratio for the beam is (from Equation 35)

$$\bar{c} = \frac{\sum_{\beta\alpha} I_{\beta\alpha}}{\sum_{\beta\alpha} \dot{m}_{\beta\alpha}} = \frac{I}{\dot{M}} = 63.8 \text{ coul/kg}$$

The dotted line in Figure 26 is the mass flow distribution if one were simply to take a current distribution and divide by 63.8 coul/kg. To determine the mass flow distribution in this way would be to assume that \bar{c} was constant at all positions in the beam and could be determined by a single TOF reading.

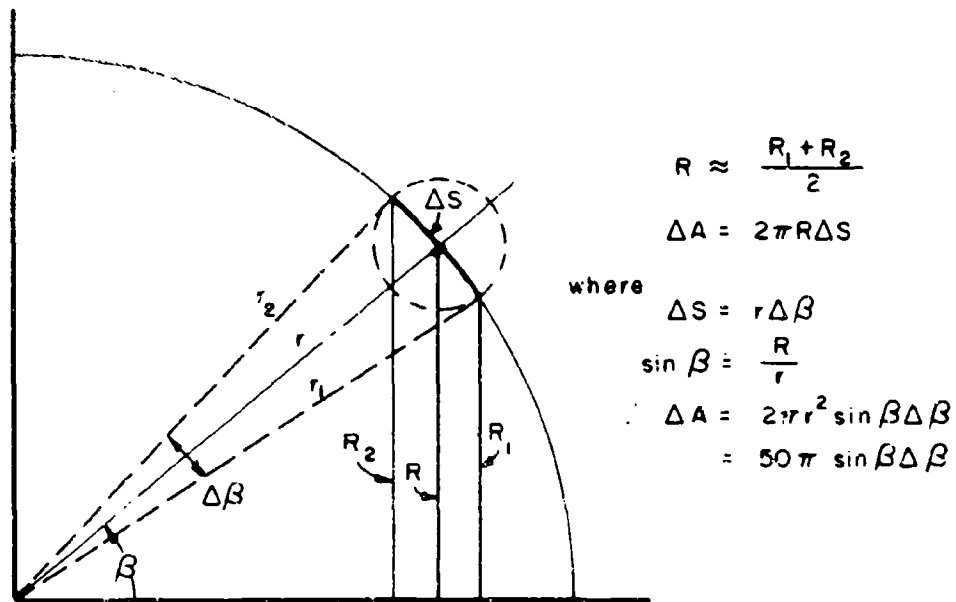


Figure 25. Determination of Surface Area of Circular Strip of Width, ΔS , and Radius, R

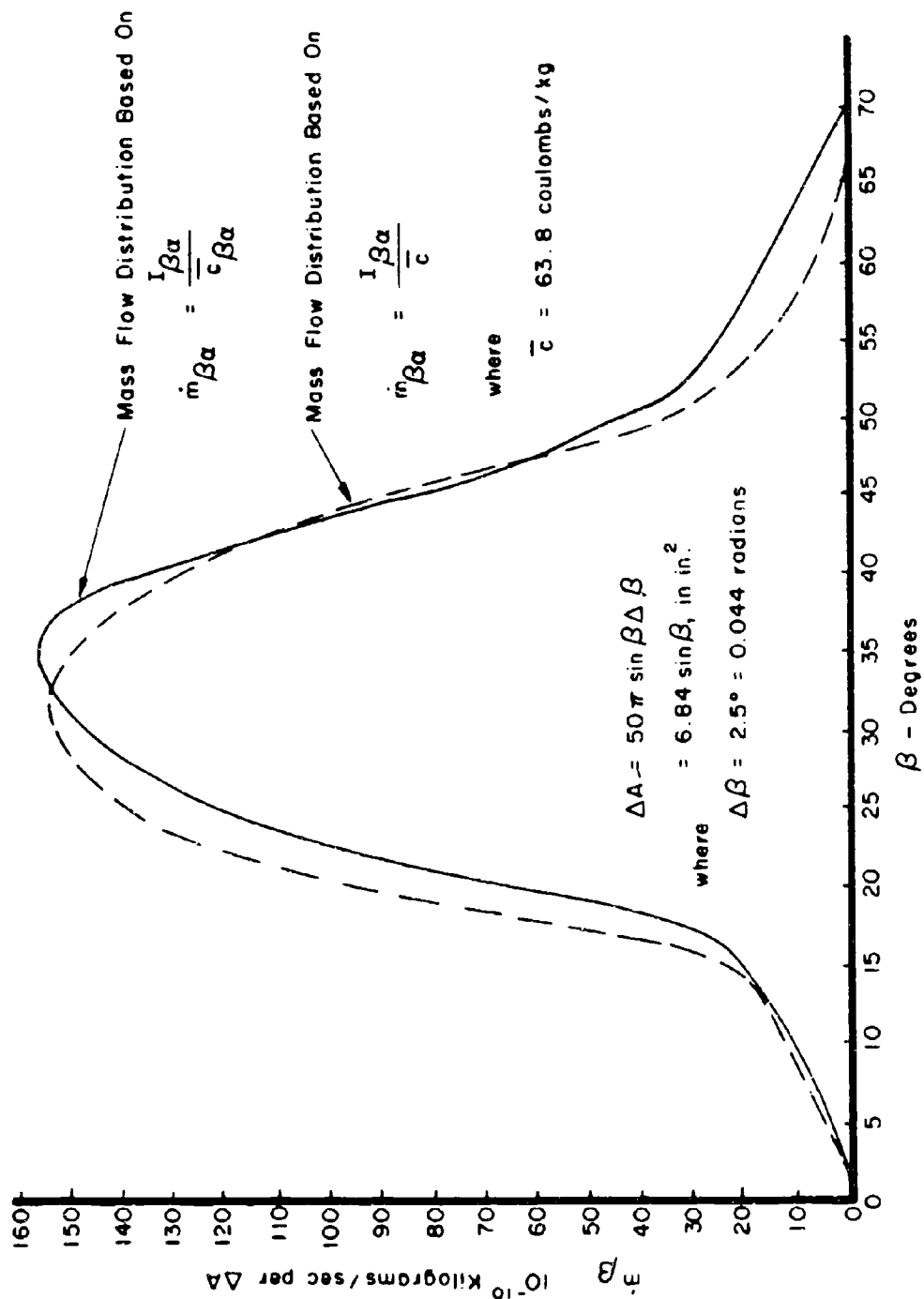


Figure 26. Propellant Mass Flow Distribution Contributed by Elemental Surface Areas, ΔA , Situated at Different Beam Divergence Angles, β

Figure 27 shows the variation of the parameters \bar{c}_β and $\bar{c}_\beta^{1/2}$, as a function of β . It has previously been shown that the specific charge varied widely with azimuthal angle (see Figure 22). There is a gradual increase in the parameters, with β out to an angle of 18° , then a gradual decrease out to $\beta = 70^\circ$. The results of Figure 27 were used when the solid line in Figure 26 was drawn. Because no beam current was measured at angles of $\beta = 0^\circ$ to 7.5° and only a negligible current was measured at $\beta = 50^\circ$ to 70° , \bar{c}_β , $\bar{c}_\beta^{1/2}$, and the current had to be interpolated in these regions by smooth curves. Therefore, this part of the \dot{m} curve in Figure 26 is not as accurate as the curve for $\beta = 7.5^\circ$ to $\beta = 50^\circ$. However, only a small fraction of the mass flow exists outside this region. The error in mass flow is estimated to be about 2%.

The correct mass flow distribution shows a shift of about 5° from the incorrect ($\bar{c} = \text{constant}$) determination.

As can be seen from Figure 26, the beam is hollow along the engine axis with the flow peaking at the half angle $\beta = 36^\circ$ and decreasing rapidly to zero at 70° . Figure 28 is a photograph of a model of the mass flow distribution of the beam determined by graphs similar to the one shown in Figure 23. The fact that the beam is hollow was verified by observing the pattern of propellant depositing on the TC collector, as shown in Figure 29. The pattern on the collector is a result of an accumulation of three individual colloid runs, all with low specific charge beams; however, on all three operations, the beam was essentially hollow. Although the photographers' lights caused a glare at the center of the hemispherical collector, little or no deposit was observed.

While the mechanics of colloid particle extraction are not completely understood, we know that the detachment point for particles at the needle rim and the departure angle depends upon the field configuration at the needle (Reference 8, 10). The field influences the shape of the fluid meniscus in the interior of the needle and the shape and departure angle of the fluid streamlets leaving the meniscus. Experimental evidence indicates that spraying occurs in a finite number of discrete jets from the meniscus, since, by varying the needle voltage, a spray consisting of several jets can be obtained. Since it has been observed that a decrease in needle voltage causes beam spread, the shape

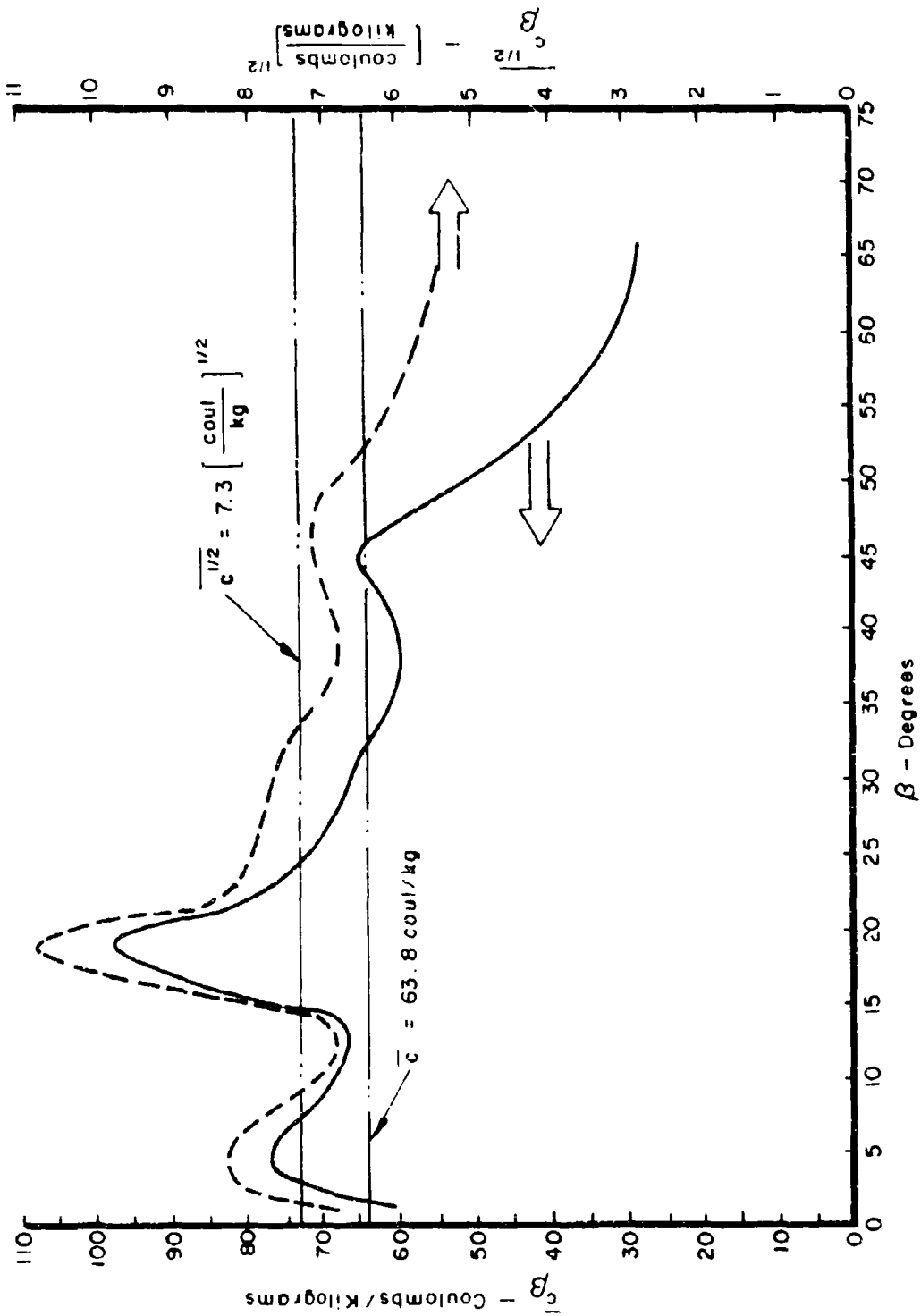


Figure 27. Mean Specific Charge \bar{c}_β , and Mean Root Specific Charge, $\bar{c}_\beta^{1/2}$, as a Function of Beam Divergence Angle, β

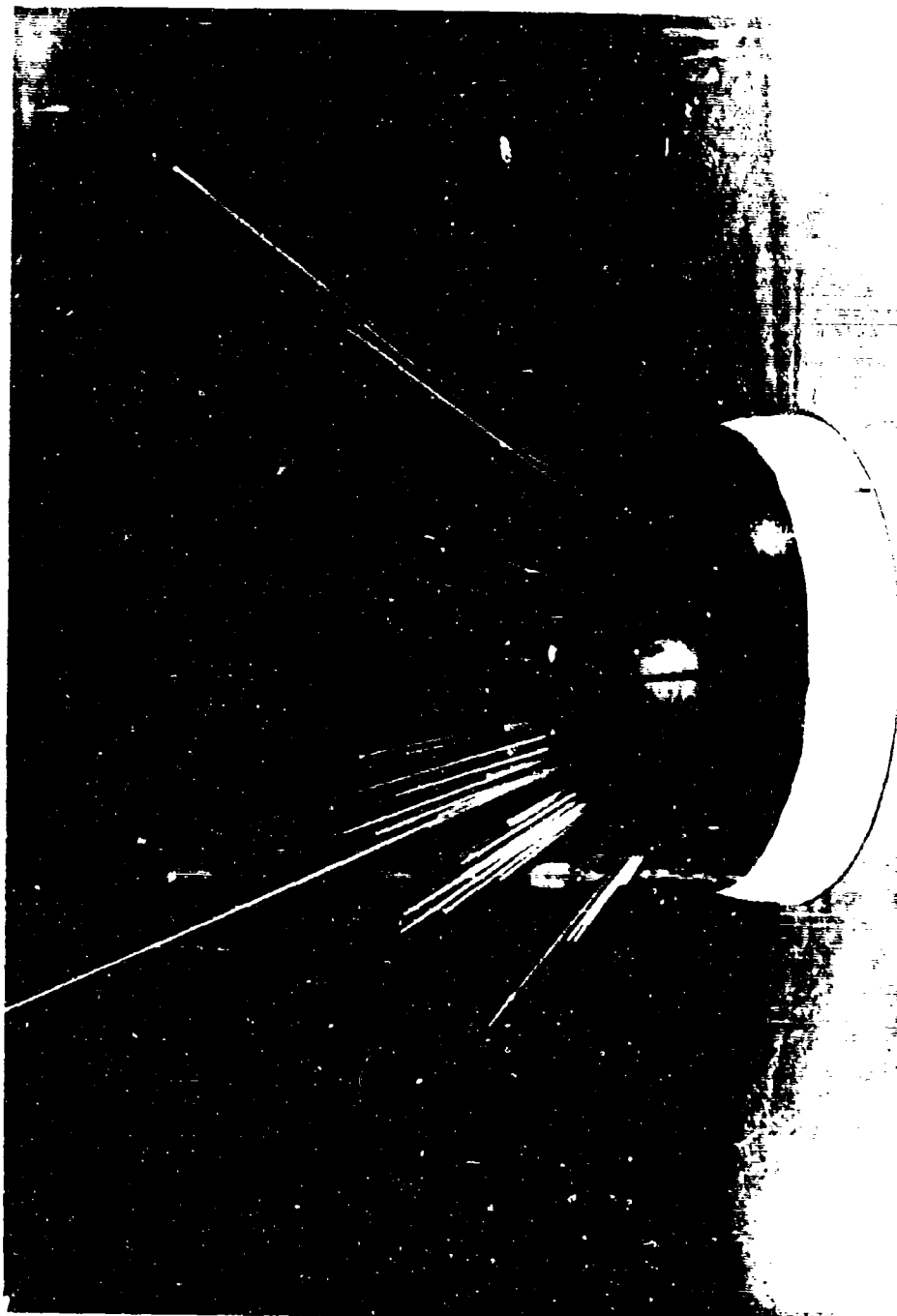


Figure 28. Model of Three-Needle Array Propellant Mass Flow Distribution.
Rods lengths are Proportional to Propellant Flow Rate



Figure 29. Pattern of Propellant Deposited on Total Current Collector

of the beam was probably influenced by a varying field strength and meniscus shape. (Reference 10.)

b. Diagnosis of Beam Characteristics

(1) Correlation of Current Readings; Determination of Droplet Size and Mass

The procedure outlined in Paragraph 2a increased the current reading determined at the ball collector from 0.55 microamperes to 1.4 microamperes. However, since the needle current microammeter read 12 microamperes, and the total current collector recorder was 4.35 microamperes, a large fraction of the current was still unaccounted for.

A determination was made of the screening effect of the secondary electrode suppressor screen that surrounded the BC collector. Two methods were used to determine the screen transparency. The hemispherical screen was made of No. 20 mesh, 0.009" dia. stainless steel. With this fact known and assuming that at the distance of 5" from the source the streams of charged particles passed parallel to each other and perpendicular to the screen, a graphical determination could be made of what fraction of the beam passed through the grid.

By cutting out the projected areas of the impinging beam on the cross section of the collector and weighing the samples, the average screen transparency was determined to be about 57%. This result was checked later by using a Photon Meter (Figure 30) to ascertain the drop in the intensity of light passing through the screen. The ratio of the intensity of light passing through a hollow tube to the intensity of light passing through the tube with the wire screen mounted on one end was $\frac{100}{55}$ to $\frac{100}{62}$. Therefore, the average transparency of the screen is the inverse, 55-62%, which agrees well with the graphic determination.

The total current collector also had a screen in front of it. While the ball current collector screen was convex spherical toward the impinging beam, the total current collector screen was concave spherical and geometrically presented a higher transparency to the beam.

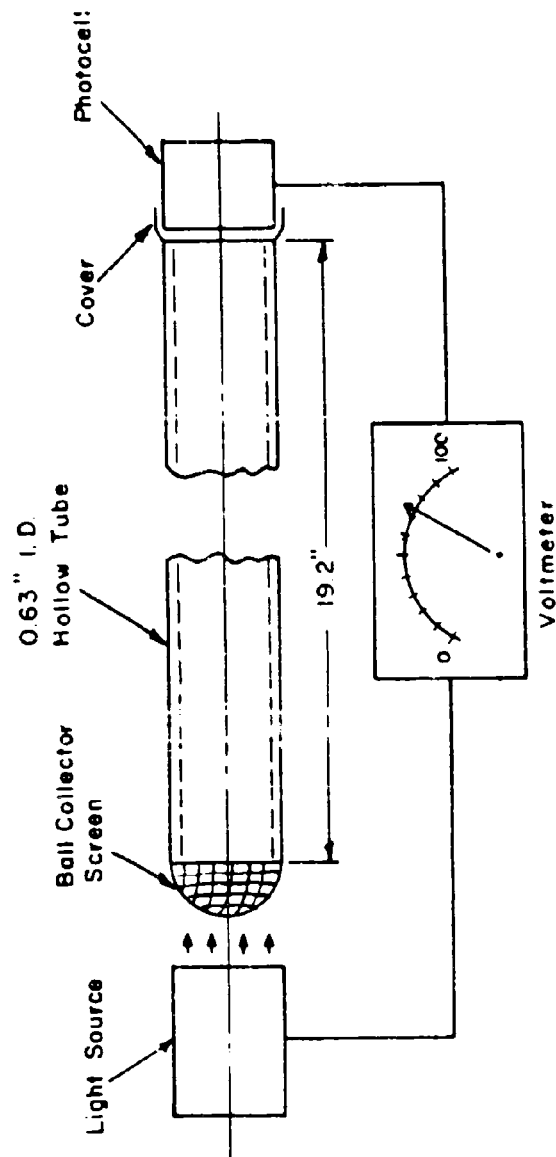


Figure 30. Photon Meter for Determining Ball Collector Screen Transparency

However, before equations could be set up relating all system currents, it was necessary to consider further the geometry of the ball collector and screen (Figure 31). The ball screen had a larger cross-sectional diameter than did the ball itself (about 0.8 inches compared to 0.57 inches) and was physically connected to a metal plate behind the ball collector, and electrically isolated from the ball. This geometrical and electrical arrangement meant that when the ion beam reached the ball collector system, part of the ions impinged on the portion of the screen outside the ball diameter, and another fraction of the beam passed through this part of the screen and struck the back metal plate.

These ion currents, outside the ball collector cross-sectional area, while not adding to the ball collector current, produce secondary electrons which go to the collector. The presence of electron current to the collector has the effect of cancelling out an equal ion current to the collector. Therefore, the ball collector would receive a greater percentage of electrons because of the current striking the entire screen and the back metal plate. It was also determined that in Region I the screen transparency was about 0.69 while in Region II it was 0.42 (overall screen transparency was 0.56).

Figure 31 illustrates what is happening. The ion current in Region II striking the screen at (B) and (C) produces additional secondary electrons that go to the collector.

Equations relating all system currents could now be set up. An electrometer, originally placed in the extractor circuit, was not functioning properly and had to be removed. Unfortunately, no microammeter had been placed in the BC and TC circuits, which obviously seriously hampers correlation of currents.

An estimate of the currents, however, can be made by calculating a value for the secondary electron coefficient γ . In Reference 11, γ has been determined experimentally to be equal to 1.25 at 5300 volts needle potential and at a particle specific charge of 7000 coulombs/kg. As a first approximation, we

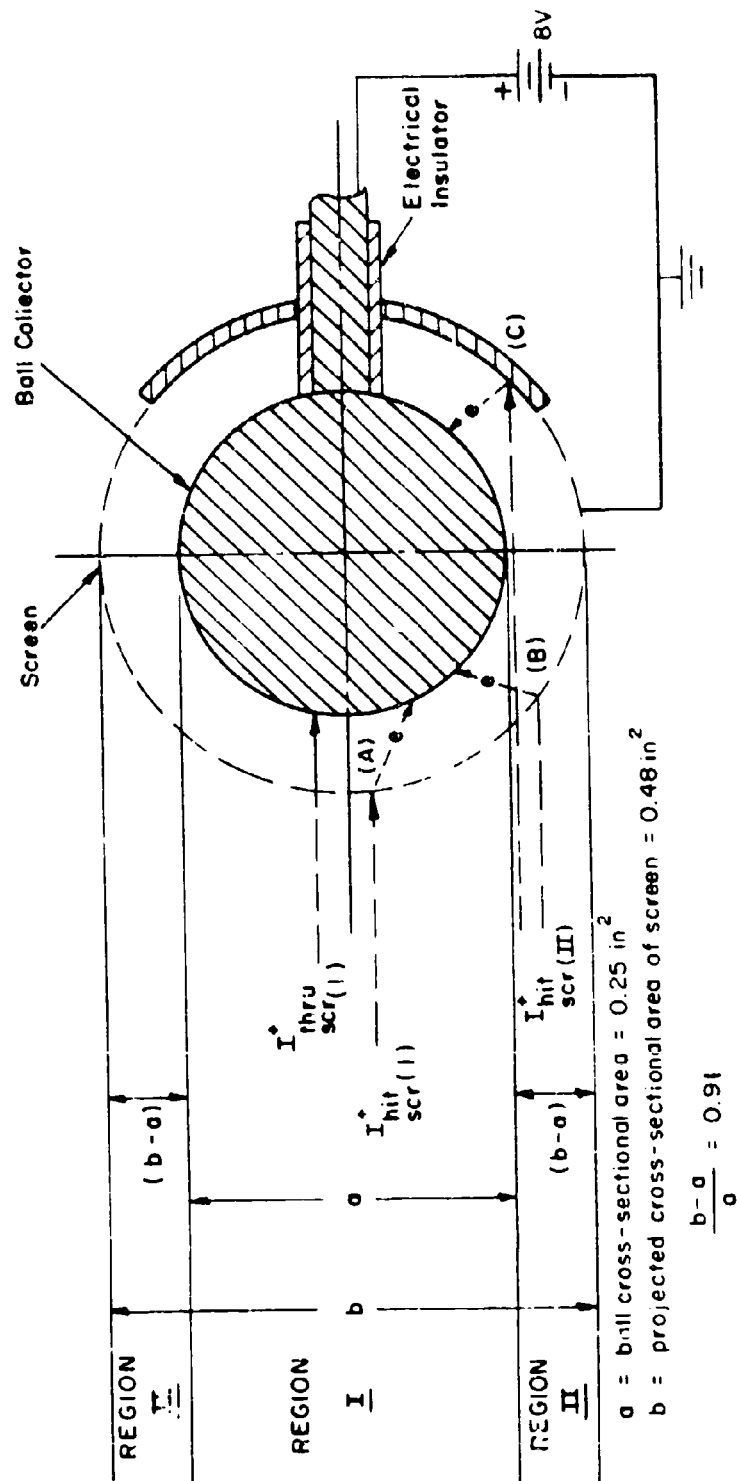


Figure 31. Schematic of Ball Current Collector Showing Regions of Charged Particle Impact

can state that the secondary electron coefficient is a function of the kinetic energy of the impinging ion for constant voltage, or $\gamma = f(m\bar{v})$. Therefore,

$$\gamma_1 = \left(\frac{m_1 \bar{c}_1}{m_2 \bar{c}_2} \right) \alpha_2 \quad (39)$$

where

$$\gamma_2 = 1.25$$

$$\bar{c}_1 = 63.8 \text{ coul/kg}$$

$$\bar{c}_2 = 7000 \text{ coul/kg}$$

where m , the mass of each droplet, can be determined by

$$m = \rho \text{Vol} = 1.26 \times 10^3 \frac{\text{kg}}{\text{m}^3} \times \frac{4}{3} \pi r^3 = 5.28 \times 10^3 r^3$$

Droplet size can be estimated with the techniques described in Reference 5, where droplet size is determined by considering the surface energy forces, coulombic forces, and field emission effects. Using the Raleigh criterion for r (Reference 5) for low specific charge particles, we find $r_1 = 10^{-7}$ meters = 1000 Å

Therefore

$$m_1 = 5.28 \times 10^{-18} \text{ kg}$$

Using the field emission limit equation for ions for high specific charge particles, we find

$$r_2 = 3 \times 10^{-8} \text{ meters} = 300 \text{ Å}$$

Therefore,

$$m_2 = 0.14 \times 10^{-18} \text{ kg}$$

By substituting in Equation (39), we find

$$\gamma_1 = 0.42$$

Using the calculated values of screen transparencies, the secondary electron coefficient and the cross-sectional area relationship, $\frac{b-a}{a} = 0.91$, the following current relationships can be found.

$$f_1 = 0.69 = I_{\text{thru}}^+ / (I_{\text{thru}}^+ + I_{\text{hit}}^+) = I_{\text{thru}}^+ / \text{Flow}(1)$$

$$\text{Flow}(1) = I_{\text{hit}}^+ + I_{\text{thru}}^+ = \left(\frac{a}{b-a} \right) \text{Flow}(2) = \left(\frac{a}{b-a} \right) I_{\text{hit}}^+(\text{II})$$

$$0.56 = \text{Flow}(1) / (\text{Flow}(1) + \text{Flow}(2))$$

$$f_2 = I_{\text{thru}}^+ / I_{\text{hit}}^+ = 0.42$$

$$I_{\text{hit}}^+(\text{II}) = I_{\text{hit}}^+(2) + I_{\text{thru}}^+(2)$$

which is based on the assumption that all currents in Region II produce secondary electrons.

By manipulating the above relationships we can find

$$I_{\text{thru}}^+ = \frac{I_{\text{BC}}}{1 - \gamma(1.765)} \quad \text{where } I_{\text{BC}} = 1.4$$

$$I_{\text{from}}^- = 0.42 I_{\text{hit}}^+$$

$$I_{\text{from}}^- = 0.42 I_{\text{hit}}^+(\text{II})$$

$$I_{\text{scr}} = I_{\text{hit}}^+ + I_{\text{from}}^-$$

$$I_{\text{ext}} = I_{\text{hit}}^+ + I_{\text{from}}^-$$

$$I_{\text{from}}^- = 0.42 I_{\text{hit}}^+$$

$$I_{\text{ext}} = I_N - \text{Flow}(1) = 12 - \text{Flow}(1)$$

$$I_{\text{total}}^+ = I_{\text{hit}}^+ + I_{\text{hit}}^+(\text{I}) + I_{\text{thru}}^+(\text{I})$$

$$I_N = 12 = I_{\text{ext}} + I_{\text{BC}} + I_{\text{scr}} + I_{\text{from}}^- = I_{\text{ext}} + I_{\text{BC}} + I_{\text{hit}}^+ + I_{\text{from}}^- + I_{\text{from}}^-$$

The calculated currents are shown in Figure 32 and are listed in Table II. It should be noted that while the total electron current from the entire screen is considered because all of it impinges on the ball collector only the ion current in the cross-sectional area of Region I (area a) is included. All previous summations to determine the total ball collector current over the spherical surface out to $\beta = 70^\circ$ were made as a function of the ball collector cross-sectional area a, and not the screen cross-sectional area b.

By using the equations for current relationships, current continuity can be shown to hold in the range of $0 \leq \gamma \leq 1$, that is, for $\gamma > 1$ several calculated current values become negative. Also, for any value of $\gamma < 1$, the calculated values of the total ion current emitted from the needle differ by less than 10%. The final calculated value of current determined by using the calculated value of $\gamma = 0.42$ is $I_{\text{total}}^+ = 10.82$ microamperes (Figure 32).

(2) Final Determination of Mass Flow Rate

The mass flow rate determined from Equation 32 is now

$$\dot{M} = \frac{10.82 \times 10^{-6}}{63.8} = 17.0 \times 10^{-8} \text{ kg/sec}$$

(3) Charge-to-Mass Ratio

Charge-to-mass ratio (specific charge) as determined on the ball collector was $\bar{c} = 63.8$ coul/kg at $V = 5300$ volts and propellant feed pressure of two inches of mercury. Propellant resistivity for the 15 grams NaI/100 ml glycerol solution was $2.9 \text{ K}\Omega\text{-cm}$ at 30°C . It has been shown (Reference 5 and 8) that the specific charge is influenced by needle voltage, needle geometry, feed system pressure, and the propellant resistivity. Generally, specific charge increases with an increase in needle voltage, and a decrease in feed pressure and resistivity, which is caused by an increased concentration of NaI in glycerol. The influence of capillary potential on specific charge for a constant feed pressure is shown in Figure 33.

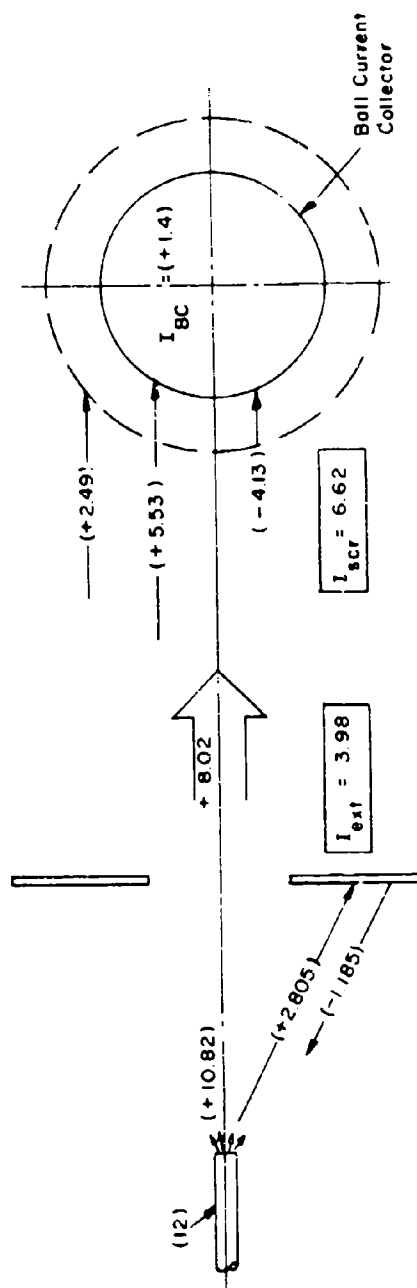
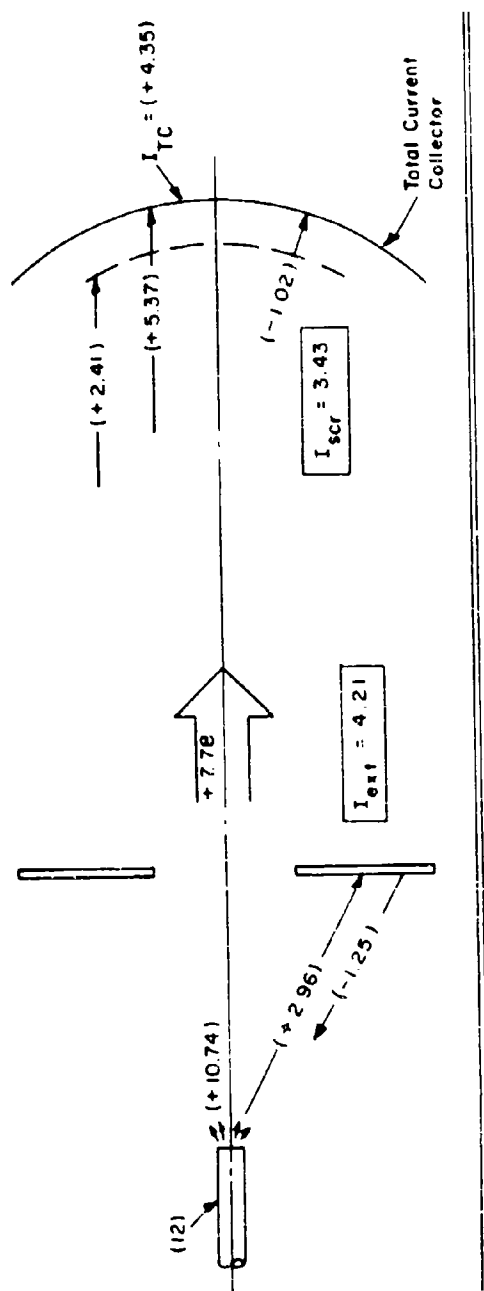


Figure 32. System Currents in Microamperes

TABLE II
SYSTEM CURRENTS

System Currents	Total Current Collector	Ball Current Collector
System Characteristics Used to Calculate System Currents		
Secondary Electron Coefficient γ	0.42	0.42
Screen Transparency, %	69	69 in Region I 42 in Region II 56 average
$\frac{b-a}{a}$	---	0.91
$I_{TC}, (\mu \text{ amps})$	4.35	---
$I_{BC}, (\mu \text{ amps})$	---	1.4
$I_N, (\mu \text{ amps})$	12	12
$I_{hit \text{ ext}}, (\mu \text{ amps})$	2.96	2.81
$I_{from \text{ ext}}, (\mu \text{ amps})$	1.25	1.19
$I_{ext}, (\mu \text{ amps})$	4.21	3.98
$I_{hit \text{ scr}}, (\mu \text{ amps})$	2.41	2.49
$I_{from \text{ scr}}, (\mu \text{ amps})$	1.02	4.13
$I_{thru \text{ scr}(1)}, (\mu \text{ amps})$	5.37	5.53
$I_{scr}, (\mu \text{ amps})$	3.43	6.62
$I_{total}, (\mu \text{ amps})$	10.74	10.82

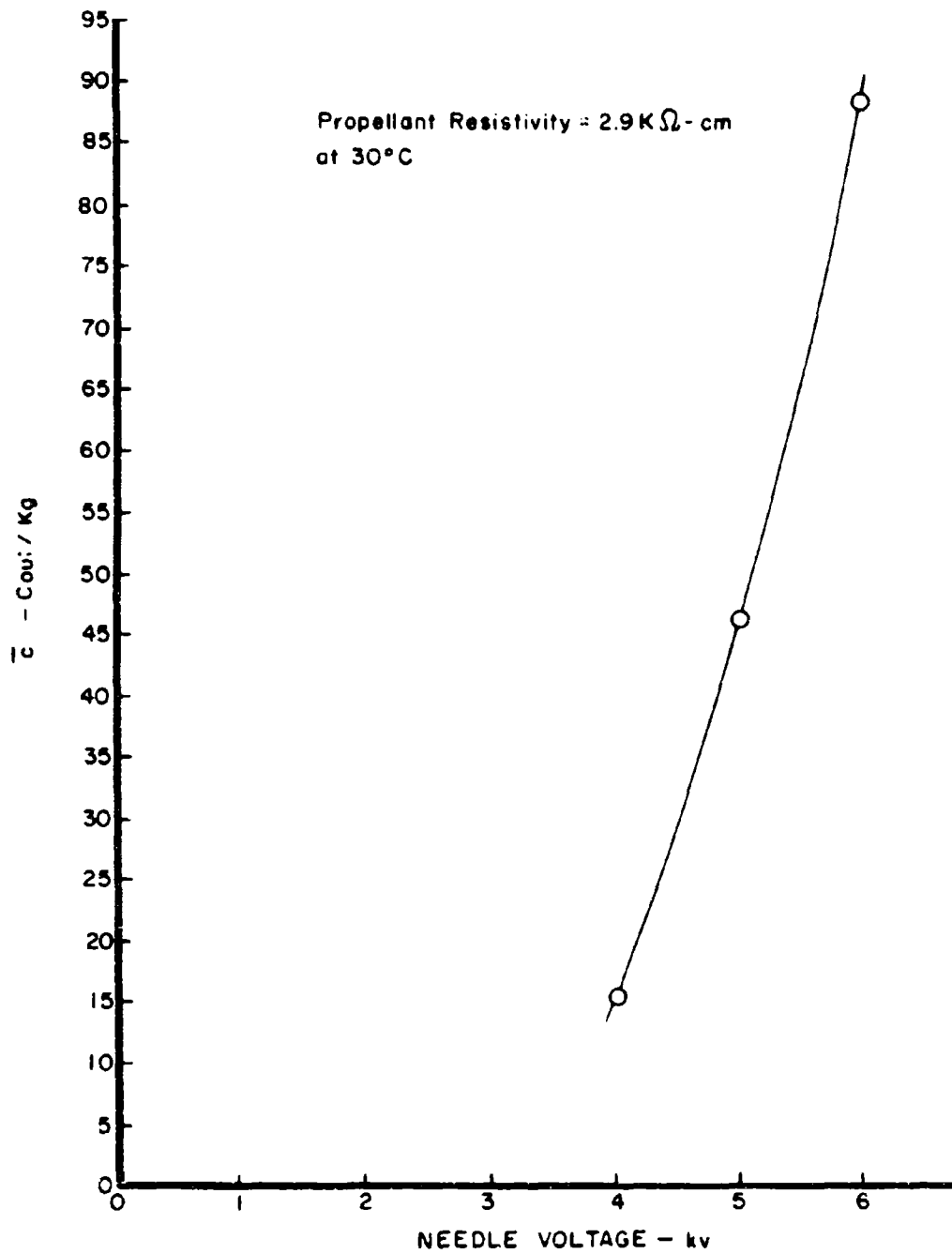


Figure 33. Influence of Needle Voltage on Specific Charge for Constant Feed System Pressure (TC, TOF, Trace)

It was impractical to operate the needles at voltages higher than about 6 kv because the TOF current traces on the ball collector became negligible or negative. It is believed that, at higher voltages, the increased secondary electron current from the ball screen to the ball masked out the ion current.

The specific charge recorded on the TC collector, at the same operating conditions (same pressure) as for the mass of data recorded at the ball collector, was $\bar{c} = 24.2$ coul/kg. The discrepancy between this value and the ball collector reading ($\bar{c} = 63.8$ coul/kg) is unexplained. However, instantaneous flow rates, as determined by TOF data, can vary from the measured average* by as much as 40% (Reference 12). A large number of time-of-flight measurements made under constant pressure and temperature conditions will agree closely with the measured average. Therefore, it is believed that the determination of \bar{c} by use of the summation ball collector TOF traces is more accurate than a single total collector TOF trace. However, it would be an interesting experiment to determine if there is any change in specific charge with TOF distance. TC TOF distance was 1.95" and BC TOF distance was 5".

(4) Neutral Particle Efflux

Although no determination of neutral particles efflux was made, long time tests conducted by the electric propulsion industry (Reference 11) have shown that neutral efflux is only the order of 1-2% and, therefore, is considered negligible. These tests were performed by comparing average instantaneous TOF mass flow rate calculations with the mass flow rate determined by actually weighing the propellant reservoir before and after a long term operation and dividing by the time. This is defined as the "measured flow rate average."

(5) Beam Divergence and Anisotropic Distribution Effects on Needle Performance

Thrust and current and mass flow were calculated similarly, i.e., by the use of Equation (30) and the graphical techniques. True thrust, taking into account the anisotropic conditions of specific charge and current and also the

*measured average is discussed in the subparagraph (4) "Neutral Particle Efflux."

beam divergence, is $F = F_x = 23.3$ micropounds. The true thrust in the axial direction, contributed by the beam as a function of divergence angle, is shown in Figure 34. If beam divergence is neglected, Equation (20) (with $\bar{c} = 63.8, c^{1/2} = 7.37$) may be used, and we get $F = 28.8$ micropounds.

If the mass flow for a thrust of 28.8 micropounds were considered to be distributed uniformly out to a half angle of $\beta = 36^\circ$ (see Figure 26), the thrust would be 26.1 micropounds.

If one were to consider that specific charge was isotropic in regard to divergence angle β , then thrust for isotropic $\bar{c}, c^{1/2}$, and divergent beam is $F = 23.9$ micropounds.

This points out that the anisotropic conditions of \bar{c} and $c^{1/2}$ as shown in Figure 27 were insignificant at the positions in the beam where beam current was significant, in that they caused little change in calculated thrust ($\sim 2.5\%$). That is, although there was a variation in \bar{c} and $c^{1/2}$ as a function of beam angle β , it occurred in regions where the beam current was small.

The fact that the beam could be considered as truly hollow as verified by using Equation (20') (where $\bar{c} = 63.8, c^{1/2} = 7.3$, and $\beta = 36^\circ$) to compute the true thrust.

The result was $F = 23.2$ micropounds compared to the graphical determination of $F = 23.3$ micropounds. The experimenter, however, would be unlikely to guess by a simple current distribution, or by observing a beam pattern on the collector such a precise angle as $\beta = 36^\circ$. However, this angle can be seen as the angle where the mass flow is greatest (Figure 26).

In conclusion, the condition of anisotropic \bar{c} and $c^{1/2}$ had a negligible effect in computing thrust, and since the beam was hollow, Equation (30), the summation thrust equation for anisotropic \bar{c} and $c^{1/2}$, current, and divergent beam, can be replaced by Equation (20'). However, if the observer assumes that the beam is uniformly distributed out to some β , rather than being hollow, his thrust calculation is considerably off (26.1 micropounds compared to the true value of 23.3 micropounds).

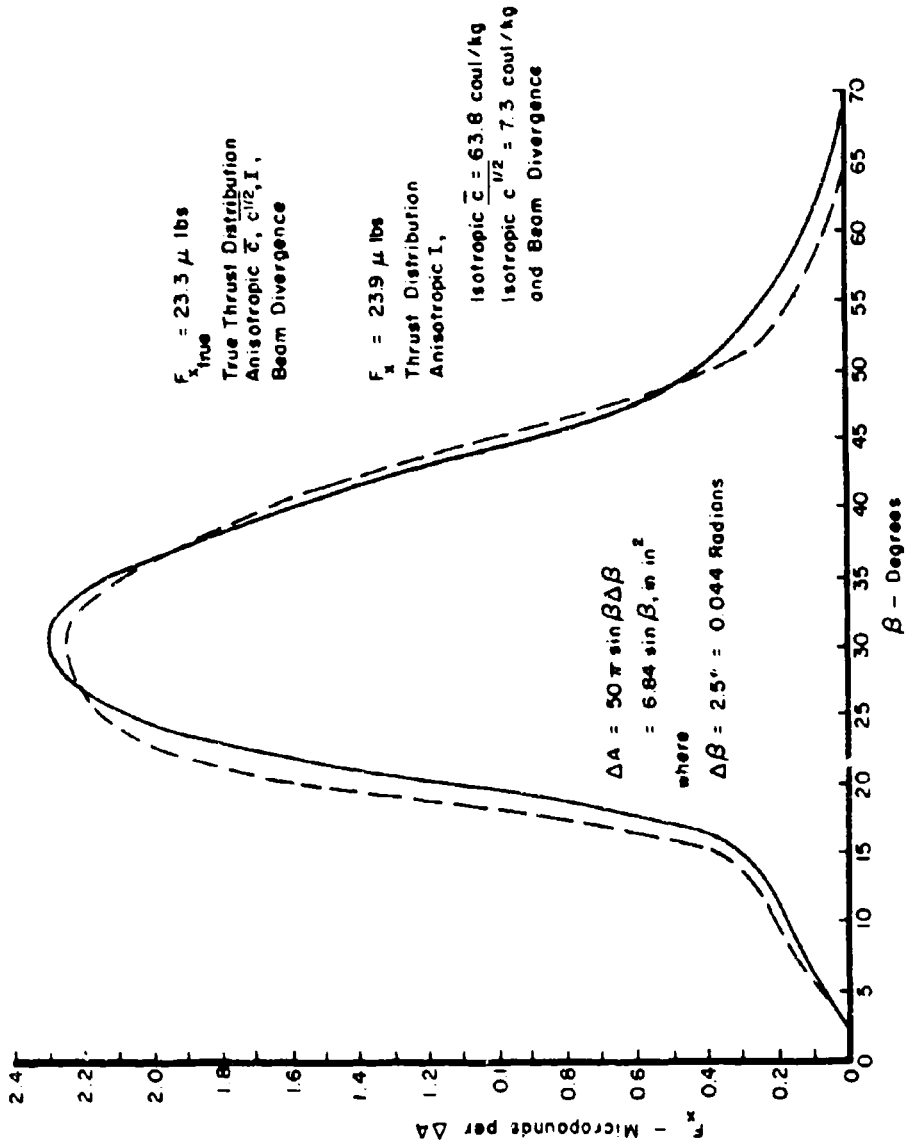


Figure 34. Thrust Distribution in Axial Direction Contributed by Elemental Surface Areas, ΔA , Situated at Different Beam Divergence Angles, β

The true value of thrust being known, we can now find the performance of the three-needle array.

We can define overall efficiency for a thruster operating in a space environment where there are no collector screens to retard ion flow and cause secondary electrons as

$$\eta_o = \frac{\eta_F \times I_{IONS}^+ V}{I_{IONS}^+ V + I_{from\ ext}^- (V - V^-)} \quad (40)$$

where

$$I_{ions}^+ = 10.82 \times 10^{-6} \text{ amps}$$

$$I_{from\ ext}^- = 1.19 \times 10^{-6} \text{ amps}$$

$$V = \text{needle voltage} = 5300 \text{ volt}$$

$$V^- = \text{extractor voltage} = -450 \text{ volts}$$

$$\therefore \eta_o = \eta_F (0.9)$$

where η_F is given by Equation (33)

$$\therefore \eta_o = 0.9 \left[\frac{F_x^2}{2 \dot{M} P_{IN}} \right] = 49.2 \%$$

total input power is

$$P_i = I_{IONS}^+ V + I_{from\ ext}^- (V - V^-) = 64.2 \times 10^{-3} \text{ watts}$$

and specific impulse (Equation 34) is

$$I_{sp} = \frac{F_x}{\dot{M} g_o} = 62 \text{ seconds}$$

As found previously, $\dot{M} = 17.0 \times 10^{-8} \text{ kg/sec}$

These are the performance parameters arrived at by assuming an anisotropic divergent beam.

AFAPL-TR-69-13

The comparison of true engine performance with performance calculated by not considering anisotropic conditions and beam divergence is shown in Table III. Table IV summarizes the calculated three-needle array performance.

TABLE III
COMPARISONS OF ENGINE PERFORMANCE BASED ON ISOTROPIC - ANISOTROPIC CONDITIONS

Techniques Used for Calculating Thrust	F (μ lbs)	Approx % Error	Isp (sec)	Approx % Error	η_F (%)	Approx % Error	η_0 (%)	Approx % Error
True Performance ₀ (anisotropic $\bar{c}, c^{1/2}, I$, and beam divergence)	23.3 (Eq 30)	---	62	---	54.3	---	48.9	---
Performance based on isotropic $\bar{c}, c^{1/2}$, anisotropic I , and beam divergence	23.9	2.5	63.5	2.5	57.2	5	51.5	5
Performance based on parallel beam (no divergence)	28.8 (Eq 20)	24	76.7	24	83	53	74.7	53
Performance based on uniform distribution of \dot{m} and beam divergence	26.1	12	69.5	12	68	25	61	25

TABLE IV
THREE-NEEDLE ARRAY PERFORMANCE AS DETERMINED FROM
BALL CURRENT COLLECTOR TOF TRACES

Performance Parameters	Results Obtained
Needle Current, I_n	12 μ amps
Positive Current, I_{total}^+	10.82 μ amps
Mean specific charge, \bar{c}	63.8 coul/kg
Mean root specific charge, $\bar{c}^{1/2}$	7.3 coul ^{1/2} /kg ^{1/2}
Total input power, P_t	64.2 x 10 ⁻³ watts
Propellant mass flow, \dot{M}	17.0 x 10 ⁻⁸ kg/sec
True thrust, F_x	23.3 μ lbs
Specific impulse, I_{sp}	62 seconds
Thrust efficiency, η_F	54.7 %
Roll Efficiency, η_o	49.2 %

SECTION VIII

CONCLUSIONS

From the analytical and experimental work performed, the following conclusions can be made:

1. Under the stated operating conditions of fluid resistivity, propellant feed pressure, and needle voltage, the generation of a low specific charge colloid beam results in an anisotropic propellant mass flow distribution that is in the form of a hollow cone with a divergence angle of $\beta = 36^\circ$. This distribution is caused primarily by a conical current distribution and is influenced to a lesser extent by a specific charge distribution which showed \bar{c} increasing from the axis of the beam out to 20° and then gradually decreasing out to 70° . These results show that assumption (c) in Section IV, Paragraph 3, made by researchers in colloid propulsion, was not correct for these operating conditions, as specific charge was shown to be anisotropic, although it had little effect on engine performance. Mass flow distribution, which is also anisotropic, cannot be ignored.
2. Under the above stated operating conditions, the calculation of engine performance can be made with Equation (30) by determining the current distribution and by holding \bar{c} and $\bar{c}^{1/2}$ constant. Both \bar{c} and $\bar{c}^{1/2}$ can be determined from a TOF total collector positioned at the same distance from the needles as the summation ball collector. For hollow beams, Equation (30) may be replaced by Equation (20') where $\eta_D = \cos^2 \beta$.
3. The anisotropic nature of the specific charge had negligible effect upon the calculation of engine performance (5% error in overall efficiency), because the greatest deviation of specific charge from the average occurred where beam current was a small fraction of the total current.
4. The propellant mass flow distribution, which was in the nature of a hollow cone, had a significant effect upon the calculation of engine performance. Assuming a uniform mass flow distribution, rather than the correct distribution, resulted in a 12% error in thrust calculation and 25% error in determining overall efficiency.

SECTION IX

RECOMMENDATIONS

The following recommendations are made:

- The influence of propellant feed pressure and needle voltage upon the formation of a hollow beam should be investigated because, from a performance standpoint, a hollow beam is the least efficient of beam shapes.
- A determination should be made of the effects, if any, of time-to-flight distance on resultant TOF specific charge determination.
- While specific charge increases with needle voltage, it is not known whether the voltage increase has any effect on the specific charge distribution with beam half angle; although it has been observed that the current distribution becomes more collimated along the beam axis.
- It is possible that at higher voltages the specific charge may still exhibit its anisotropic nature, but this phenomenon may now occur in regions of high current where it could more significantly influence mass flow distribution.

AFAPL-TR-69-13

APPENDIX

DIGITAL COMPUTER PROGRAM DEVELOPED FOR
CALCULATING COLLOID ENGINE PERFORMANCE

MAIPRO - EFN SOURCE STATEMENT - IFN(S) - 02/06/58

```

REAL ISP, IBETAL
DIMENSION COBETA(200), CBA1(200), CBA12(200), IBETAL(200)
1, Y(200), VO(200)
COMMON Y
COMMON KCBARS
DATA G/9.8/,
101 FORMAT (15)
102 FORMAT (6E12.5, 1E8.1)
103 FORMAT (1H0)
101 FORMAT (1H1, 12X, 2HFX, 12X, 3HPIN, 11X, 4HMOOT, 13X, 2HYN, 12X, 3HISP,
2 11X, -HCBAR// (6E15.5))
106 FORMAT (1H1)
107 FORMAT (E12.5, 15)
109 FORMAT (1H0, 4X, 5HDBETA=, E12.5, 5X, 7HDCOSBET=, E15.8, 5X, 2HX=, E12.5, 5X,
12HR=, E12.5)
104 FORMAT (5X, 6HALPHA=, E12.5)
READ(5, 101) KCBARS
READ(5, 101) NUMFIN
READ(5, 102) A, B, C, P
H=57.2957795
SU1=0.0
SU2=0.0
SU3=0.0
SUMTOP=0.0
SUMBOT=0.0
DO 104 NUM=1, NUMFIN
READ(5, 107) BETA, J
S=5.*SIN(BETA/H)
X=5.*COS(BETA/H)
COSBET=X/5.
WRITE (6, 100)
DO 405 K=1, J
READ (5, 101) N
READ(5, 102) ALPHA, D, V, (Y(I), I=1, N)
WRITE(6, 109) BETA, COSBET, X, R
WRITE (6, 103)
WRITE(6, 404) ALPHA
WRITE (6, 103)
CALL AAAAAA(A, B, C, D, V, P, G, N, T4, T5)
IF(KCBARS.NE.1) GO TO 402
KCBARS=2
GO TO 104
402 COBETA(K)=COSBET
CBA12(K)=T4
CBA1(K)=T5
IBETAL(K)=D
VO(K)=V
SU1=SU1+(IBETAL(K)*CBA12(K)*COBETA(K))/CBA1(K)*SQRT(2.*VO(K))
SU2=SU2+IBETAL(K)*VO(K)
SU3=SU3+IBETAL(K)/CBA1(K)
SUMTOP=SUMTOP+IBETAL(K)*CBA1(K)
SUMBOT=SUMBOT+IBETAL(K)
405 CONTINUE
104 CONTINUE
FX=SU1

```

MAIPRO - EFN SOURCE STATEMENT - IFN(S) -

02/06/68

```
FXSQ=FX**2
PIN=SU2
DOTM=SU3
XN=FXSQ/(2.*DOTM*PIN)
ISP=FX/(DOTM*G)
CBAR=SUMTOP/SUMBOT
WRITE (6,401) FX,PIN,DOTM,XN,ISP,CBAR
STOP
END
```

(64)

02/06/68

AAA - EFN SOURCE STATEMENT - IEN(S) -

SUBROUTINE AAAAAA(A,B,C,D,V,P,G,N,T4,T5)

DIMENSION Y(200)

COMMON Y

COMMON KCBARS

IF(KCBARS.NE.2) GO TO 1

T4=CBRX12

T5=CBARX1

GO TO 6

1 Y1=Y(1)/2.0

DO 2 N1=2,N

Y1=Y1+Y(N1)

2 CONTINUE

T=((((A*B)*C)/D)*Y1)*(2.54/60.0)

Y2=Y(1)/4.0

DO 3 N1=2,N

VN=N1-1

Y2=Y2+(VN*Y(N1))

3 CONTINUE

T2=(((((2.0*A)*(B**2))*(C**2))/D)*Y2)*(2.54/60.0)

T3=((P**2)*(T**2))/((2.0*V)*(T2**2))

4 T4=SQRT(T3)

IF(KCBARS.EQ.1) CBRX12=T4

T5=(P**2)/((2.0*V)*T2)

IF(KCBARS.EQ.1) CBARX1=T5

5 T6=(T**2)/T2

T7=(P*T)/(G*T2)

T8=((2.0*V)*D)*T2/(P**2)

T9=((D*(SQRT(2.0*V)))*T4)/T5

WRITE(6,301) T,T2,T3,T4,T5,T6,T7,T8,T9

IF(KCBARS.EQ.1) WRITE(6,302)

6 RETURN

301 FORMAT (1H0,12X,1HT,12X,2HT2,12X,2HT3,12X,2HT4,12X,2HT5,12X,

1 2HT6,12X,2HT7,12X,2HT8,12X,2HT9/(9E14.5)/1H0)

302 FORMAT (1H0,20X,81HSINGLE T.C. I.O.F. TRACE. T4 AND T5 ARE SAVED

IFOR USE IN FOLLOWING CALCULATIONS.)

END

REFERENCES

1. Jack W. Geis. Areas of Applicability for Electric Propulsion Systems, AFAPL-TR-67-80. Air Force Aero Propulsion Laboratory, Wright-Patterson Air Force Base, Ohio. September 1967.
2. E. Cohen. Research on Charged Colloid Generation, APL-TDR-64-75. Prepared under Contract AF33(657)-10999 by TRW Space Technology Laboratories, Redondo Beach, California. June 1964.
3. W. C. Burson, Jr. Research on Electrohydrodynamic Charged Droplet Beams, AFAPL-TR-67-109. Air Force Aero Propulsion Laboratory, Wright-Patterson Air Force Base, Ohio. October 1967.
4. R. D. Present. Kinetic Theory of Gases. McGraw-Hill, New York. Chapter 2. 1958.
5. S. H. Wineland, W. C. Burson, Jr., R. E. Hunter. The Electrohydrodynamic Generation of Charged Droplet Beams, AFAPL-TR-66-72. Air Force Aero Propulsion Laboratory, Wright-Patterson Air Force Base, Ohio. August 1966.
6. Robert E. Hunter. Exploring the Feasibility of the Electrodeless Thruster. The Ohio State University. Ph.D. Dissertation. 1965.
7. J. G. Beynon, E. Cohen, D. S. Goldin, M. N. Huberman, P. W. Kidd, and S. Zafran. "Present Status of Colloid Microthruster Technology." TRW, Inc., Redondo Beach, California. AIAA Paper No. 67-531. 1967.
8. R. E. Hunter and S. H. Wineland. "Charged Colloid Generation Research." Air Force Aero Propulsion Laboratory. Presented to the Space Electronics Symposium 25-27 May 1965. Los Angeles, California.
9. G. E. F. Sherwood and A. E. Taylor. Calculus (Mean-Value Theorem for Integrals). Prentice-Hall Inc., Englewood Cliffs, New Jersey. 1954.
10. Technical Data submitted by TRW, Inc. and discussed with Air Force Aero Propulsion Laboratory personnel.
11. M. N. Huberman and Ernest Cohen. Research on Charged Particle Electrostatic Thrusters, Volume I, Technical, AFAPL-TR-67-115. TRW Systems, Redondo Beach, California. September 1967.
12. S. Zafran, J. G. Beynon, E. Cohen. "Colloid Microthruster System Development." TRW Systems Group, Redondo Beach, California. AIAA Paper No. 68-84. AIAA 6th Aerospace Sciences Meeting, New York, New York, January 1968.

UNCLASSIFIED
Security Classification

DOCUMENT CONTROL DATA - R&D		
(Security classification of title, body of abstract and indexing annotation must be entered when the overall report is classified)		
1. ORIGINATING ACTIVITY (Corporate author) Air Force Aero Propulsion Laboratory Wright-Patterson Air Force Base, Ohio		2a. REPORT SECURITY CLASSIFICATION UNCLASSIFIED 2b. GROUP
3. REPORT TITLE DIAGNOSTICS OF A LOW-SPECIFIC-CHARGE COLLOID ION BEAM		
4. DESCRIPTIVE NOTES (Type of report and inclusive dates)		
5. AUTHOR(S) (Last name, first name, initial) Jack W. Gels		
6. REPORT DATE June 1969	7a. TOTAL NO. OF PAGES 90	7b. NO. OF REFS 12
8a. CONTRACT OR GRANT NO. a. PROJECT NO. 3141 c. Task No. 314102 d.	8b. ORIGINATOR'S REPORT NUMBER(S) AFAPL-TR-69-13 8c. OTHER REPORT NO(S) (Any other numbers that may be assigned this report)	
10. AVAILABILITY/LIMITATION NOTICES This document has been approved for public release and sale; its distribution is unlimited.		
11. SUPPLEMENTARY NOTES	12. SPONSORING MILITARY ACTIVITY Air Force Aero Propulsion Laboratory Wright-Patterson Air Force Base, Ohio	
13. ABSTRACT As part of an in-house colloid diagnostic program, the first detailed mapping of propellant mass flow distribution from a colloid source has been completed, and the program has shown the influence of anisotropic or non-uniform flow conditions within the beam on the efficiency of source operation. The operating conditions of high propellant feed pressure, low voltage, and high resistivity of the sodium iodide/glycerol propellant, which created a very low specific charge beam, caused a nonuniform distribution of specific charge and beam current as a function of beam divergence half angle. The assumption of uniform beam conditions would result in a 12% error in computing thrust and a 25% error in determining overall efficiency.		

DD FORM 1473
1 JAN 64

UNCLASSIFIED
Security Classification

UNCLASSIFIED
Security Classification

14 KEY WORDS	LINK A		LINK B		LINK C	
	ROLE	WT	ROLE	WT	ROLE	WT
Colloid Engine Electrical Propulsion Ion						

INSTRUCTIONS

1. **ORIGINATING ACTIVITY:** Enter the name and address of the contractor, subcontractor, grantee, Department of Defense activity or other organization (*corporate author*) issuing the report.
- 2a. **REPORT SECURITY CLASSIFICATION:** Enter the overall security classification of the report. Indicate whether "Restricted Data" is included. Marking is to be in accordance with appropriate security regulations.
- 2b. **GROUP:** Automatic downgrading is specified in DoD Directive 5200.10 and Armed Forces Industrial Manual. Enter the group number. Also, when applicable, show that optional markings have been used for Group 3 and Group 4 as authorized.
3. **REPORT TITLE:** Enter the complete report title in all capital letters. Titles in all cases should be unclassified. If a meaningful title cannot be selected without classification, show title classification in all capitals in parenthesis immediately following the title.
4. **DESCRIPTIVE NOTES:** If appropriate, enter the type of report, e.g., interim, progress, summary, annual, or final. Give the inclusive dates when a specific reporting period is covered.
5. **AUTHOR(S):** Enter the name(s) of author(s) as shown on or in the report. Enter last name, first name, middle initial. If military, show rank and branch of service. The name of the principal author is an absolute minimum requirement.
6. **REPORT DATE:** Enter the date of the report as day, month, year, or month, year. If more than one date appears on the report, use date of publication.
- 7a. **TOTAL NUMBER OF PAGES:** The total page count should follow normal pagination procedures, i.e., enter the number of pages containing information.
- 7b. **NUMBER OF REFERENCES:** Enter the total number of references cited in the report.
- 8a. **CONTRACT OR GRANT NUMBER:** If appropriate, enter the applicable number of the contract or grant under which the report was written.
- 8b, 8c, & 8d. **PROJECT NUMBER:** Enter the appropriate military department identification, such as project number, subproject number, system numbers, task number, etc.
- 9a. **ORIGINATOR'S REPORT NUMBER(S):** Enter the official report number by which the document will be identified and controlled by the originating activity. This number must be unique to this report.
- 9b. **OTHER REPORT NUMBER(S):** If the report has been assigned any other report numbers (*either by the originator or by the sponsor*), also enter this number(s).
10. **AVAILABILITY/LIMITATION NOTICES:** Enter any limitations on further dissemination of the report, other than those

imposed by security classification, using standard statements such as:

- (1) "Qualified requesters may obtain copies of this report from DDC."
- (2) "Foreign announcement and dissemination of this report by DDC is not authorized."
- (3) "U. S. Government agencies may obtain copies of this report directly from DDC. Other qualified DDC users shall request through _____."
- (4) "U. S. military agencies may obtain copies of this report directly from DDC. Other qualified users shall request through _____."
- (5) "All distribution of this report is controlled. Qualified DDC users shall request through _____."

If the report has been furnished to the Office of Technical Services, Department of Commerce, for sale to the public, indicate this fact and enter the price, if known.

11. **SUPPLEMENTARY NOTES:** Use for additional explanatory notes.

12. **SPONSORING MILITARY ACTIVITY:** Enter the name of the departmental project office or laboratory sponsoring (*paying for*) the research and development. Include address.

13. **ABSTRACT:** Enter an abstract giving a brief and factual summary of the document indicative of the report, even though it may also appear elsewhere in the body of the technical report. If additional space is required, a continuation sheet shall be attached.

It is highly desirable that the abstract of classified reports be unclassified. Each paragraph of the abstract shall end with an indication of the military security classification of the information in the paragraph, represented as (TS), (S), (C), or (U).

There is no limitation on the length of the abstract. However, the suggested length is from 150 to 225 words.

14. **KEY WORDS:** Key words are technically meaningful terms or short phrases that characterize a report and may be used as index entries for cataloging the report. Key words must be selected so that no security classification is required. Identifiers, such as equipment model designation, trade name, military project code name, geographic location, may be used as key words but will be followed by an indication of technical context. The assignment of links, rules, and weights is optional.

UNCLASSIFIED
Security Classification